

## Article

# Petrogenesis of the Newly Discovered Neoproterozoic Adakitic Rock in Bure Area, Western Ethiopia Shield: Implication for the Pan-African Tectonic Evolution

Junsheng Jiang <sup>1,2</sup> , Wenshuai Xiang <sup>1,\*</sup>, Peng Hu <sup>1,\*</sup>, Yulin Li <sup>3</sup>, Fafu Wu <sup>1</sup>, Guoping Zeng <sup>1</sup>, Xinran Guo <sup>4</sup>, Zicheng Zhang <sup>5</sup> and Yang Bai <sup>6</sup>

<sup>1</sup> Wuhan Center, China Geological Survey (Central South China Innovation Center for Geosciences), Wuhan 430205, China; jsjiang0818@163.com (J.J.)

<sup>2</sup> Research Center for Petrogenesis and Mineralization of Granitoid Rocks, China Geological Survey, Wuhan 430205, China

<sup>3</sup> Institute of Geological Survey, China University of Geosciences, Wuhan 430074, China; a942186394@gmail.com

<sup>4</sup> The Geological Science Education Center of Guangdong, Guangzhou 510000, China; xinran5566@163.com

<sup>5</sup> China National Geological & Mining Corporation, Beijing 100029, China; zhangzicheng@chinagm.com.cn

<sup>6</sup> Geophysical Exploration Brigade HuBei Geological Bureau, Wuhan 430056, China

\* Correspondence: xiangwenshuai@mail.cgs.gov.cn (W.X.); hpeng@mail.cgs.gov.cn (P.H.)

**Abstract:** The Neoproterozoic Bure adakitic rock in the western Ethiopia shield is a newly discovered magmatic rock type. However, the physicochemical conditions during its formation, and its source characteristics are still not clear, restricting a full understanding of its petrogenesis and geodynamic evolution. In this study, in order to shed light on the physicochemical conditions during rock formation and provide further constraints on the petrogenesis of the Bure adakitic rock, we conduct electron microprobe analysis on K-feldspar, plagioclase, and biotite. Additionally, we investigate the trace elements and Hf isotopes of zircon, and the Sr-Nd isotopes of the whole rock. The results show that the K-feldspar is orthoclase ( $Or = 89.08\sim 96.37$ ), the plagioclase is oligoclase ( $Ab = 74.63\sim 85.99$ ), and the biotite is magnesio-biotite. Based on the biotite analysis results, we calculate that the pressure during rock formation was 1.75~2.81 kbar (average value of 2.09 kbar), representing a depth of approximately 6.39~10.2 km (average value of 7.60 km). The zircon thermometer yields a crystallization temperature of 659~814 °C. Most of the  $(Ce/Ce^*)_D$  values in the zircons plotted above the Ni-NiO oxygen buffer pair, and the calculated magmatic oxygen fugacity ( $\log fO_2$ ) values vary from  $-18.5$  to  $-4.9$ , revealing a relatively high magma oxygen fugacity. The uniform contents of FeO, MgO, and K<sub>2</sub>O in the biotite suggest a crustal magma source for the Bure adakitic rock. The relatively low  $(^{87}Sr/^{86}Sr)_i$  values of 0.70088 to 0.70275, positive  $\epsilon_{Nd}(t)$  values of 3.26 to 7.28, together with the positive  $\epsilon_{Hf}(t)$  values of 7.64~12.99, suggest that the magma was sourced from a Neoproterozoic juvenile crust, with no discernable involvement of a pre-Neoproterozoic continental crust, which is coeval with early magmatic stages in the Arabian Nubian Shield elsewhere. Additionally, the mean Nd model ages demonstrate an increasing trend from the northern parts (Egypt, Sudan, Afif terrane of Arabia, and Eritrea and northern Ethiopia; 0.87 Ga) to the central parts (Western Ethiopia shield; 1.03 Ga) and southern parts (Southern Ethiopia Shield, 1.13 Ga; Kenya, 1.2 Ga) of the East African Orogen, which indicate an increasing contribution of pre-Pan-African crust towards the southern part of the East African Orogen. Based on the negative correlation between MgO and Al<sub>2</sub>O<sub>3</sub> in the biotite, together with the Lu/Hf-Y and Yb-Y results of the zircon, we infer that the Bure adakitic rock was formed in an arc-arc collision orogenic environment. Combining this inference with the whole rock geochemistry and U-Pb age of the Bure adakitic rock, we further propose that the rock is the product of thickened juvenile crust melting triggered by the Neoproterozoic Pan-African Orogeny.

**Keywords:** Bure adakitic rock; mineralogical characteristics; Sr-Nd-Hf isotopes; Western Ethiopia Shield



**Citation:** Jiang, J.; Xiang, W.; Hu, P.; Li, Y.; Wu, F.; Zeng, G.; Guo, X.; Zhang, Z.; Bai, Y. Petrogenesis of the Newly Discovered Neoproterozoic Adakitic Rock in Bure Area, Western Ethiopia Shield: Implication for the Pan-African Tectonic Evolution. *Minerals* **2024**, *14*, 408. <https://doi.org/10.3390/min14040408>

Academic Editors: Ignez de Pinho Guimarães and Jefferson Valdemiro De Lima

Received: 21 February 2024

Revised: 4 April 2024

Accepted: 9 April 2024

Published: 16 April 2024



**Copyright:** © 2024 by the authors. Licensee MDPI, Basel, Switzerland. This article is an open access article distributed under the terms and conditions of the Creative Commons Attribution (CC BY) license (<https://creativecommons.org/licenses/by/4.0/>).

## 1. Introduction

The East African Orogen (EAO) has recorded a complex history of intra-oceanic and continental margin magmatic and tectono–thermal events from the Neoproterozoic to the Early Cambrian. It mainly consists of the juvenile Arabian Nubian Shield (ANS) and the largely older continental crust of the Mozambique Belt (MB) from north to south [1–3]. The Western Ethiopian Shield (WES) is situated in a key location, relatively close to the transition between the Arabian Nubian Shield and the Mozambique Belt. It is also adjacent to and east of the ‘Eastern Saharan Meta-craton’ [4]. It is a metamorphic terrane that includes high-grade gneisses and low-grade metavolcanic and metasedimentary rocks with associated intrusions. The granitoid rocks, which have either intruded into greenschist facies volcano–sedimentary sequences or been emplaced at the contact between low- and high-grade terranes, constitute a significant proportion of plutonic rocks in the Precambrian rocks of the WES. Many researchers have focused on the granitoid rocks in the WES, significantly advancing our understanding of regional tectonic evolution [5–11]. However, the magma source of these granitoid rocks in the WES, especially those intruding into the low- and high-grade rock associations within the eastern part of the WES, remains unclear. Also unclear is whether the magma source derived from mixing with pre-Neoproterozoic crustal material or not.

The Bure granite in the WES formed in the Pan-African Orogeny Period (750–650 Ma; [5]). It has an LA-ICP-MS U-Pb age of  $773.8 \pm 8.1$  Ma and is characterized by high Sr (310~401 ppm), Sr/Y (64.9~113.6), and La/Yb (25.7~51.6), and low MgO (0.27~0.41 wt%), Y (2.71~4.78 ppm), and Yb (0.20~0.31 ppm) values [7]. Based on the study by Xu et al. [12], Jiang et al. [7] defined the Bure granite as an adakitic rock. This rock is called the Bure adakitic rock in this study. It is a newly discovered magmatic rock type in this area. However, the magma source and physicochemical conditions of the Bure adakitic rock remain unknown, hindering a comprehensive understanding of its petrogenesis and geodynamic evolution during the Pan-African period. Its mineralogical and isotopic compositions vary significantly depending on the type of precursor rocks and/or igneous processes during the evolution of its parental magma. Thus, knowledge of the mode of origin of these rocks contributes to our understanding of the Neoproterozoic evolutionary history of the WES.

This study investigates the major elements of typical minerals (K-feldspar, plagioclase, and biotite), trace elements and Hf isotopes of zircon, and Sr-Nd isotopes of the whole rock from the Bure adakitic rock in the eastern part of the WES. Combined with local and regional geological, geochemical, and geochronological data, the results shed light on the degree of pre-Neoproterozoic crustal material involvement in the source magmas, and the Neoproterozoic geological evolution of the WES.

## 2. Geological Setting

The EAO is a Neoproterozoic to early Cambrian mobile belt that reflects the collision between Neoproterozoic India and the African Neoproterozoic continents [1,2,13,14]. Based on its lithological and metamorphic characteristics, the EAO can be broadly subdivided into two terranes, the Arabian Nubian Shield in the north and the Mozambique Belt in the south. The ANS is dominated by low-grade volcano–sedimentary rocks associated with plutons and ophiolitic remnants [4,15–19], and represents the juvenile terrane. However, the MB in the south part of the EAO is a tract of largely older continental crust that was extensively deformed and metamorphosed in the Neoproterozoic/Cambrian ([10,20–22]; Figure 1).

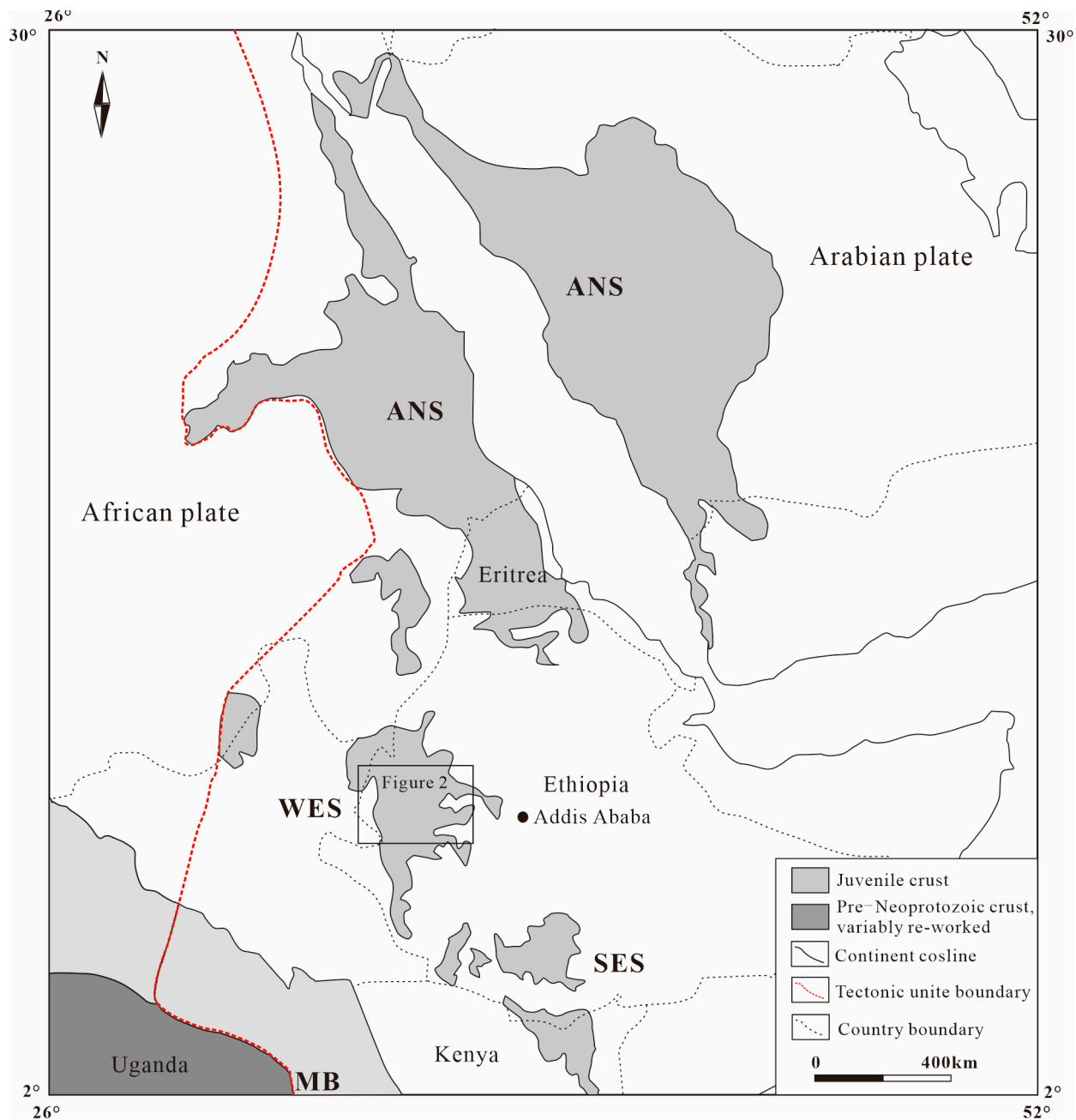


**Figure 1.** Geological map of the Arabian-Nubian Shield, northeast Africa (after [14]).

The WES is also called the Tulu-dimtu Orogenic Belt, which is understood to have formed during the amalgamation of western Gondwana before the final closure of the Mozambique Ocean [15]. It can be subdivided into five litho-tectonic domains from west to east—the Daka, Sirkole, Dengi, Kemashi, and Didesa Domains. The Daka Domain lies in the southwest corner of the WES (Figure 2) and consists of pre-Neoproterozoic basement gneisses representing the western basement margin of the Tulu-dimtu Belt. The Sirkole Domain, composed of gneissic and volcano-sedimentary rocks intruded by granites, is located in the northwestern portion of the WES that extends into Sudan. The Dengi Domain is characterized by a deformed and metamorphosed volcano-sedimentary sequence and the Jamoa-Ganti orthogneiss; there are several intrusive bodies in this domain. It is generally thought to be a volcanic arc sequence related to the closure of the ocean represented by the Tulu-dimtu Ophiolite to the east. The Kemashi Domain consists of a sequence of metasedimentary rocks and abundant mafic to ultra-mafic volcanic material that has

been metamorphosed to upper greenschist/epidote-amphibolite facies. The nature of these ultra-mafic/mafic plutonic rocks within the Kemashi Domain is controversial, with some scholars holding that they represent an ophiolite sequence [4,15,23], named the Tulu Dimtu Ophiolite. However, others [24–26] hold that these ultra-mafic/mafic plutonic rocks represent Alaskan-type, concentrically zoned intrusions, which were emplaced into an extensional arc or back-arc environment. The Didesa Domain within the eastern boundary of the WES is characterized by amphibolite facies paragneiss and orthogneiss intruded by Neoproterozoic intrusive rocks. It is located in the transition between the Arabian Nubian Shield and the Mozambique Belt.

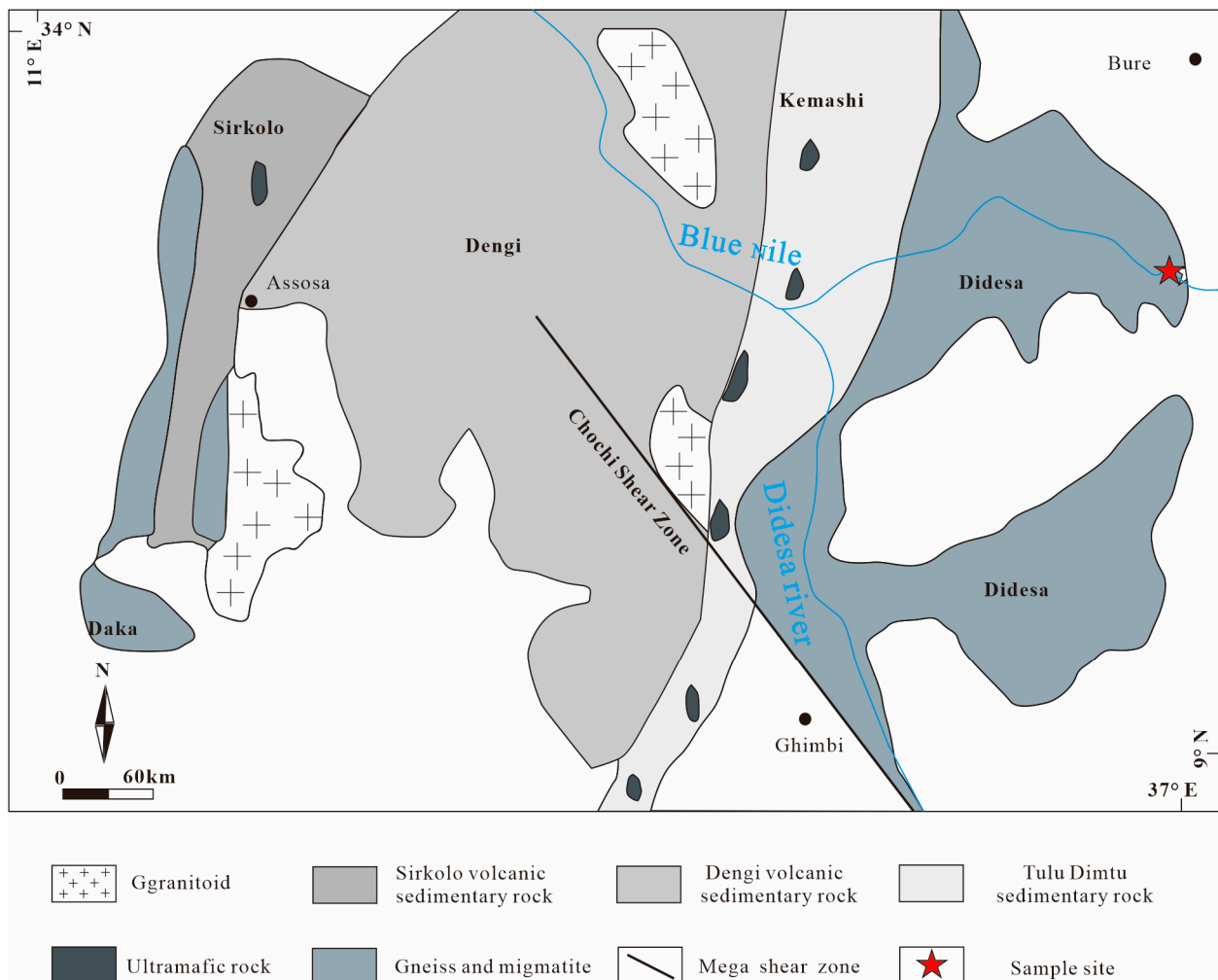


**Figure 2.** Sketch of the regional geology of the western Ethiopian terrain (after [15]).

Three generations of magmatism at ca. 850–810 Ma, 780–700 Ma, and 650–550 Ma [5,8–10,27,28], which represent pre-, syn-, and post-tectonic environments, respectively, have been recognized by previously limited ages from elsewhere in the WES [10,21]. These intrusions are usually present as strains and dikes and are developed as ductile fault contact or intrusive contact with the surrounding rock. The main types of intrusions are granite, granodiorite, monzogranite, and tonalite. The Bure adakitic rock is located at the eastern boundary of the Didesa Domain, with the surrounding rocks comprising gneisses. This rock assemblage suggests that it not only inherited the unique rock assemblages of the Arabic-Nubian Shield but also developed the typical middle-high grade metamorphic rocks of the Mozambique Belt.

### 3. Samples and Analytical Methods

#### 3.1. Petrography

The Bure adakitic rock appears light gray in the field, with a fine granitic texture. It is mainly composed of K-feldspar (45–48 wt%), plagioclase (20–23 wt%), quartz (23–25 wt%), biotite (4–5 wt%), and minor amounts of muscovite (1–2 wt%) (Figure 3a). The K-feldspar is heteromorphic granular, with a size of 0.2–1.5 mm, some of which show slight kaolinization on the surface. The plagioclase is granular and 0.1 to 1 mm in size, with characteristics of polysynthetic twins and Carlsbadal bite compound twins. The surface of the plagioclase is usually altered, displaying light sericitization. The quartz is xenomorphic-granular, with a size of 0.05–0.7 mm (Figure 3b).

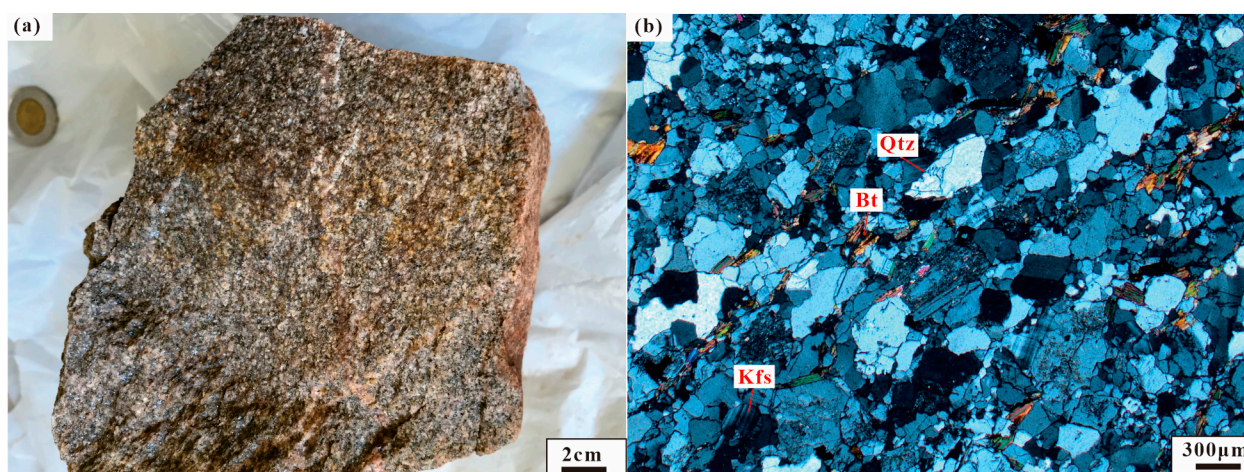


**Figure 3.** Hand specimen photograph (a) and microphotograph (b) for the Bure adakitic rock. Qtz—quartz; Bt—biotite; Kfs—K-feldspar.

#### 3.2. Analytical Methods

Electron microprobe analysis (EMPA) was performed on the K-feldspar, plagioclase, and biotite at the Zhongnan Mineral Resources Supervision and Test Center for Geoanalysis, Wuhan Center, China Geological Survey. During the analysis, a 10-μm spot size was used for the plagioclase and K-feldspar, and a 1-μm spot size was used for the biotite, with an accelerating voltage of 20 kV and a beam current of 20 nA. The integration times for the Ti and Mn peaks were 20 s and that for the remaining elements was 10 s. The SPI and ZBA mineral standards and ZAF calibration were employed for all minerals.

Trace element analyses of zircon were conducted synchronously using LA-ICP-MS at the Wuhan Sample Solution Analytical Technology Co., Ltd. Laser sampling was performed using a GeolasPro laser ablation system consisting of a COMPexPro 102 ArF excimer laser (wavelength of 193 nm and maximum energy of 200 mJ) and a MicroLas optical system. An Agilent 7700e ICP-MS instrument was used to acquire ion-signal intensities. Zircon 91,500 and glass NIST610 were used as external standards for trace element calibration. Helium was applied as a carrier gas. Argon was used as the make-up gas and mixed with the carrier gas via a T-connector before entering the ICP. The spot size and frequency of the laser were set to 32 μm and 10 Hz, respectively. Each analysis incorporated a background acquisition of approximately 20–30 s followed by 50 s of data acquisition from the sample. Excel-based software ICPMSDataCal 11.8 was used to perform quantitative calibration for trace element analysis [29].

About 0.1–0.2 g of whole rock powder of each sample was dissolved in digestion bombs with a mixture of double distilled HNO<sub>3</sub>, HF, and HClO<sub>4</sub>. They were then placed in an electric oven and heated to 190 °C for 48 h. Columns of DoweAG50WX8 and HDEHP resin were used successively for the separation and purification of rare earth elements (REEs) and finally for the separation of Nd and Sm by HCl eluant. The Sr-Nd isotopic

measurements were performed using the Triton Ti thermal ionization mass spectrometer (TIMS) at the Laboratory of Isotope Geochemistry, Wuhan Center of China Geological Survey.  $^{143}\text{Nd}/^{144}\text{Nd}$  and  $^{87}\text{Sr}/^{86}\text{Sr}$  ratios were normalized to  $^{143}\text{Nd}/^{144}\text{Nd} = 0.7219$  and  $^{87}\text{Sr}/^{86}\text{Sr} = 8.375209$ , respectively. Measurements of the La Jolla and SRM NBS987 standards during this course gave average  $^{143}\text{Nd}/^{144}\text{Nd}$  and  $^{87}\text{Sr}/^{86}\text{Sr}$  ratios of  $0.511847 \pm 3$  ( $2\sigma$ ,  $n = 25$ ) and  $0.710254 \pm 8$  ( $2\sigma$ ,  $n = 22$ ), respectively.  $^{147}\text{Sm}/^{144}\text{Nd}$  and  $^{87}\text{Rb}/^{86}\text{Sr}$  ratios of the samples were calculated using Sm, Nd, Rb and Sr concentrations as measured by the ICP-MS, and their relative uncertainties are  $\sim 0.3\%$  and  $\sim 1\%$ , respectively, based on USGS standard analyses [30].

In situ Hf isotope ratio analysis was conducted using a Neptune Plus MC-ICP-MS (Thermo Fisher Scientific, Dreieich, Germany) in combination with a Geolas HD excimer ArF laser ablation system (Coherent, Göttingen, Germany) at the Wuhan Sample Solution Analytical Technology Co., Ltd., Hubei, China. A single spot ablation mode at a spot size of  $44 \mu\text{m}$  was used, and the energy density of the laser ablation was  $\sim 7.0 \text{ J}\cdot\text{cm}^{-2}$ . Each measurement consisted of 20 s of acquisition of the background signal followed by 50 s of ablation signal acquisition. The detailed operating conditions of the laser ablation system and the MC-ICP-MS instrument and analytical method are the same as described by [31]. The normalized  $^{179}\text{Hf}/^{177}\text{Hf} = 0.7325$  and  $^{173}\text{Yb}/^{171}\text{Yb} = 1.132685$  were used to calculate the mass bias of Hf ( $\beta\text{Hf}$ ) and Yb ( $\beta\text{Yb}$ ), respectively [32]. The interference of  $^{176}\text{Yb}$  on  $^{176}\text{Hf}$  was corrected by measuring the interference-free  $^{173}\text{Yb}$  isotope and using  $^{176}\text{Yb}/^{173}\text{Yb} = 0.79639$  to calculate  $^{176}\text{Yb}/^{177}\text{Hf}$  [31]. Similarly, the relatively minor interference of  $^{176}\text{Lu}$  on  $^{176}\text{Hf}$  was corrected by measuring the intensity of the interference-free  $^{175}\text{Lu}$  isotope and using the recommended  $^{176}\text{Lu}/^{175}\text{Lu} = 0.02656$  to calculate  $^{176}\text{Lu}/^{177}\text{Hf}$ . Off-line selection and integration of analyte signals and mass bias calibrations were performed using ICPMSDataCal [33]. In order to ensure the reliability of the analysis data, three international zircon standards of Plešovice, 91,500, and GJ-1 were analyzed simultaneously with the actual samples. Plešovice was used for the external standard calibration to further optimize the analysis and test results. 91,500 and GJ-1 were used as the second standard to monitor the quality of data correction. The external precision (2SD) of Plešovice, 91,500, and GJ-1 was better than 0.000020. The test value is consistent with the recommended value within the error range. At the same time, we used the internationally recognized high Yb/Hf ratio standard sample, Temora 2, to monitor the test data of the high Yb/Hf ratio zircon. The Hf isotopic compositions of Plešovice, 91,500, and GJ-1 have been reported by Zhang et al. [34].

## 4. Results

### 4.1. Mineral Compositions

#### 4.1.1. K-Feldspar

The K-feldspar crystals of the Bure adakitic rock show relatively uniform compositional variation in the major elements (Table 1), with 11.23–16.66 wt% of  $\text{K}_2\text{O}$  (average value of 15.74 wt%), 0.37–1.20 wt% of  $\text{Na}_2\text{O}$  (average value of 0.62 wt%), and 10.81–19.36 wt% of  $\text{Al}_2\text{O}_3$  (average value of 18.51 wt%). The low contents of CaO, MgO,  $\text{TiO}_2$ , and MnO indicate that there is less isomorphism and the formation temperature of K-feldspar is low [35]. The orthoclase (Or) value is high (89.08–96.37), the albite (Ab) value is low (3.57–10.59), and the anorthite (An) value is almost negligible (0–0.38), suggesting that the K-feldspar in this area is orthoclase (Figure 4a). The Or and  $\text{Al}_2\text{O}_3$  values in the K-feldspar crystal show the same zigzag variation trend from the core to the edge, but the content of the whole porphyry is relatively stable (Figure 5a,b). This shows that the physical and chemical conditions during the formation of the potassium feldspar did not change much.

**Table 1.** Electron microprobe composition of K-felspar (wt%) for the Bure adakitic rock.

Ele.	Grt8-3 -fs01	Grt8-3 -fs02	Grt8-3 -fs04	Grt8-5 -fs01	Grt8-5 -fs02	Grt8-5 -fs04	Grt8-5 -fs05	Grt8-5 -fs06	Grt8-5 -fs07	Grt8-5 -fs08	Grt8-5 -fs09	Grt3-1 -fs01	Grt3-1 -fs02	Grt3-1 -fs03	Grt3-1 -fs04	Grt3-1 -fs05	Grt3-1 -fs06	Grt3-5 -fs07	Grt3-5 -fs08	
CaO		0.042	0.022	0.016	0.041		0.042	0.035	0.012	0.011		0.01	0.02	0.03	0.03		0.03	0.03	0.01	
Na <sub>2</sub> O	0.648	0.629	0.858	0.555	0.462	0.658	0.586	0.537	0.607	0.387	0.507	0.70	0.74	0.68	0.60	0.79	0.84	0.66	0.75	
K <sub>2</sub> O	16.085	15.769	15.465	16.152	16.66	16.136	15.93	16.026	14.227	15.874	15.892	16.28	16.07	15.74	16.34	15.91	15.61	16.10	15.02	
SrO																				
TFeO																				
MgO																				
SiO <sub>2</sub>	64.565	63.241	64.184	65.094	63.424	63.986	63.244	63.48	67.125	63.714	66.579	64.10	64.08	63.72	63.11	64.49	65.81	65.34	64.98	
MnO																				
Al <sub>2</sub> O <sub>3</sub>	19.002	18.788	18.486	19.02	19.106	19.144	18.528	19.086	19.045	19.023	17.944	18.65	17.95	18.16	18.24	18.43	18.65	18.83	18.55	
BaO																				
Total	100.30	98.47	99.02	100.84	99.69	99.92	98.33	99.16	101.02	99.01	100.92	99.74	98.87	98.34	98.32	99.61	100.94	100.95	99.30	
	Number of cation on basis of 8 oxygens																			
Si	5.950	5.938	5.979	5.963	5.909	5.926	5.952	5.923	6.047	5.942	6.070	5.954	6.000	5.987	5.957	5.983	6.003	5.977	6.008	
Al	1.548	1.559	1.522	1.540	1.573	1.567	1.541	1.574	1.517	1.568	1.446	1.531	1.486	1.509	1.522	1.511	1.504	1.523	1.516	
Mg	0.000	0.000	0.000	0.000	0.000	0.000	0.000	0.000	0.000	0.000	0.000	0.000	0.000	0.000	0.000	0.000	0.000	0.000	0.000	
Fe	0.000	0.000	0.000	0.000	0.000	0.000	0.000	0.000	0.000	0.000	0.000	0.000	0.000	0.000	0.000	0.000	0.000	0.000	0.000	
Mn	0.000	0.000	0.000	0.000	0.000	0.000	0.000	0.000	0.000	0.000	0.000	0.000	0.000	0.000	0.000	0.000	0.000	0.000	0.000	
Ca	0.000	0.002	0.001	0.001	0.002	0.000	0.002	0.002	0.001	0.001	0.000	0.000	0.001	0.002	0.001	0.000	0.001	0.001	0.000	
Na	0.029	0.029	0.039	0.025	0.021	0.030	0.027	0.024	0.027	0.017	0.022	0.031	0.034	0.031	0.028	0.035	0.037	0.029	0.034	
K	0.473	0.472	0.459	0.472	0.495	0.477	0.478	0.477	0.409	0.472	0.462	0.482	0.480	0.472	0.492	0.471	0.454	0.470	0.443	
Sr	0.000	0.000	0.000	0.000	0.000	0.000	0.000	0.000	0.000	0.000	0.000	0.000	0.000	0.000	0.000	0.000	0.000	0.000	0.000	
Ba	0.000	0.000	0.000	0.000	0.000	0.000	0.000	0.000	0.000	0.000	0.000	0.000	0.000	0.000	0.000	0.000	0.000	0.000	0.000	
An	0.0	0.2	0.1	0.1	0.2	0.0	0.2	0.2	0.1	0.1	0.0	0.0	0.2	0.1	0.0	0.1	0.1	0.1	0.0	
Ab	5.8	5.7	7.8	5.0	4.0	5.8	5.3	4.8	6.1	3.6	4.6	6.1	6.5	6.2	5.3	7.0	7.5	5.8	7.0	
Or	94.2	94.1	92.1	95.0	95.8	94.2	94.5	95.0	93.8	96.4	95.4	93.9	93.4	93.7	94.6	93.0	92.3	94.0	92.9	
Ele.	Grt3-4 -fs01	Grt3-4 -fs02	Grt3-4 -fs03	Grt3-4 -fs04	Grt3-4 -fs05	Grt3-4 -fs06	Grt3-4 -fs07	Grt3-3 -fs05	Grt3-3 -fs06	Grt3-3 -fs07	Grt3-3 -fs08	Grt3-3 -fs09	Grt3-5 -fs01	Grt3-5 -fs02	Grt3-5 -fs03	Grt3-5 -fs04	Grt3-5 -fs05	Grt3-5 -fs06	Grt3-5 -fs07	Grt3-5 -fs08
CaO	0.01	0.03	0.01	0.01	0.02	0.02		0.02	0.02	0.03	0.01	0.03	0.07	0.03	0.01	0.03	0.03	0.07	0.03	0.01
Na <sub>2</sub> O	0.55	0.51	0.58	0.57	0.61	0.60	0.55	0.52	0.61	0.68	0.51	0.46	1.20	0.70	0.56	0.62	0.84	0.70	0.66	0.75
K <sub>2</sub> O	16.19	15.61	16.46	16.29	16.16	16.55	16.19	15.96	16.44	15.78	16.43	16.35	15.37	15.88	16.02	15.91	15.44	15.75	16.10	15.02
SrO																				
TFeO																				
MgO																				
SiO <sub>2</sub>	64.79	62.78	64.62	65.35	66.01	65.06	65.05	65.06	65.78	64.51	64.68	64.55	62.67	64.95	64.78	65.80	63.77	62.82	65.34	64.98
MnO																				
Al <sub>2</sub> O <sub>3</sub>	18.80	18.78	18.75	18.91	18.53	18.53	19.25	18.81	18.81	18.31	18.43	18.55	18.99	19.05	19.08	19.07	18.33	18.93	18.83	18.55
BaO																				
Total	100.34	97.71	100.40	101.13	101.33	100.76	101.04	100.36	101.67	99.31	100.06	99.93	98.30	100.61	100.44	101.43	98.40	98.27	100.95	99.30
	Number of cation on basis of 8 oxygens																			
Si	5.969	5.935	5.961	5.972	6.011	5.981	5.948	5.980	5.983	5.996	5.985	5.977	5.900	5.958	5.955	5.979	5.980	5.916	5.977	6.008
Al	1.531	1.570	1.529	1.527	1.492	1.506	1.556	1.528	1.513	1.504	1.507	1.518	1.580	1.545	1.550	1.531	1.519	1.575	1.523	1.516
Mg	0.000	0.000	0.000	0.000	0.000	0.000	0.000	0.000	0.000	0.000	0.000	0.000	0.000	0.000	0.000	0.000	0.000	0.000	0.000	0.000
Fe	0.000	0.000	0.000	0.000	0.000	0.000	0.000	0.000	0.000	0.000	0.000	0.000	0.000	0.000	0.000	0.000	0.000	0.000	0.000	0.000
Mn	0.000	0.000	0.000	0.000	0.000	0.000	0.000	0.000	0.000	0.000	0.000	0.000	0.000	0.000	0.000	0.000	0.000	0.000	0.000	0.000
Ca	0.000	0.002	0.000	0.001	0.001	0.001	0.000	0.001	0.001	0.001	0.001	0.001	0.003	0.001	0.000	0.001	0.001	0.004	0.001	0.000
Na	0.025	0.024	0.026	0.025	0.027	0.027	0.024	0.023	0.027	0.031	0.023	0.020	0.055	0.031	0.025	0.027	0.038	0.032	0.029	0.034
K	0.476	0.470	0.484	0.475	0.469	0.485	0.472	0.468	0.477	0.468	0.485	0.483	0.461	0.465	0.470	0.461	0.462	0.473	0.470	0.443
Sr	0.000	0.000	0.000	0.000	0.000	0.000	0.000	0.000	0.000	0.000	0.000	0.000	0.000	0.000	0.000	0.000	0.000	0.000	0.000	0.000
Ba	0.000	0.000	0.000	0.000	0.000	0.000	0.000	0.000	0.000	0.000	0.000	0.000	0.000	0.000	0.000	0.000	0.000	0.000	0.000	0.000
An	0.0	0.2	0.0	0.1	0.1	0.1	0.0	0.1	0.1	0.1	0.1	0.1	0.3	0.1	0.0	0.1	0.1	0.3	0.1	0.0
Ab	4.9	4.8	5.0	5.0	5.4	5.2	4.9	4.7	5.3	6.2	4.5	4.1	10.6	6.3	5.0	5.6	7.6	6.3	5.8	7.0
Or	95.0	95.1	94.9	94.9	94.5	94.7	95.1	95.2	94.6	93.7	95.4	95.8	89.1	93.6	95.0	94.3	92.3	93.3	94.0	92.9

Note: Blank space is below the detection limit.

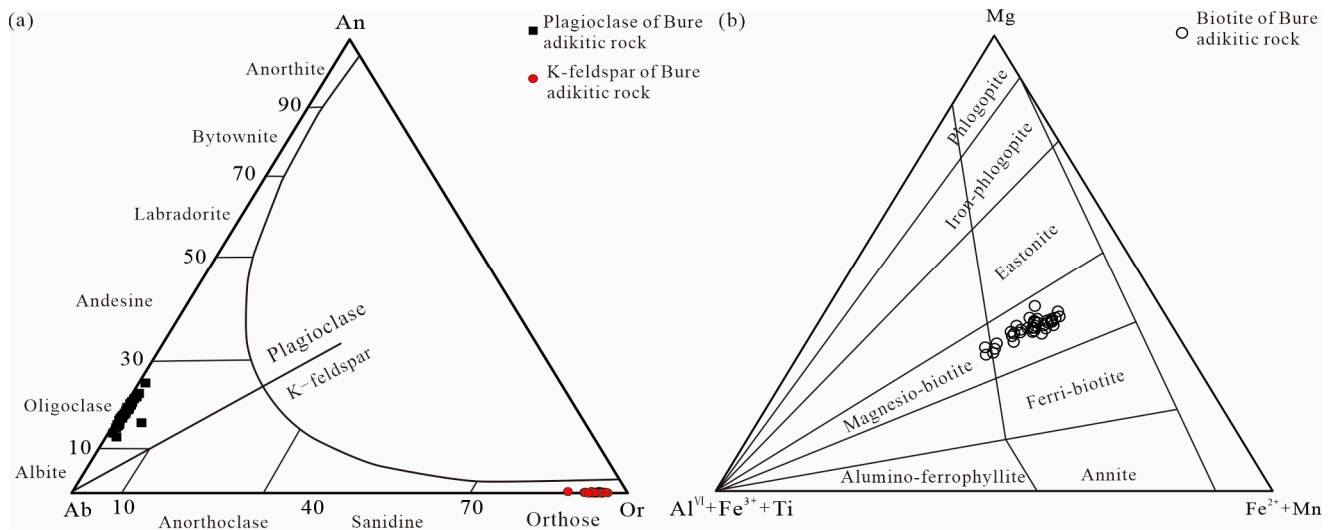


Figure 4. Ternary classification diagram for feldspar (a), [36]; Mg-(Al<sup>VI</sup> + Fe<sup>3+</sup> + Ti)-(Fe<sup>2+</sup> + Mn) classification diagram for biotite (b), [37].

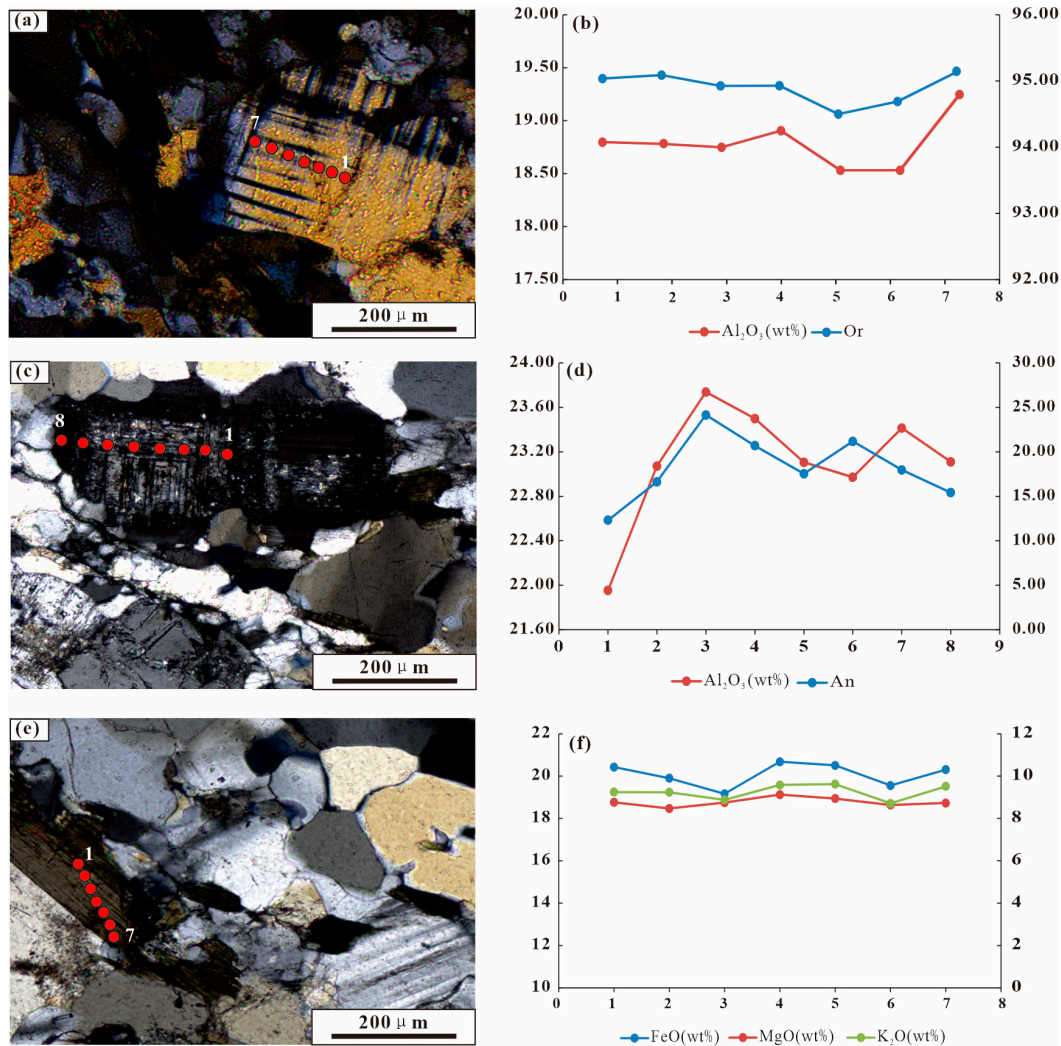


Figure 5. Electron microprobe line profile analysis of K-feldspar (a,b), plagioclase (c,d) and biotite (e,f) for the Bure adakitic rock.

#### 4.1.2. Plagioclase

The major elements in the plagioclase crystals of the Bure adakitic rock show a small range of compositions (Table 2). The SiO<sub>2</sub> content is relatively high, ranging from 62.57 to 67.75 wt% (average value of 65.18 wt%), with small variations of 6.71–10.02 wt% of Na<sub>2</sub>O (average value of 8.88 wt%), 0.09–0.74 wt% of K<sub>2</sub>O (average value of 0.16 wt%), and 2.52–4.28 wt% of CaO (average value of 3.51 wt%). In addition, the contents of FeO, MnO, and MgO in the plagioclase are below the detection limits. The Ab has high values of 74.63–85.99 (average value = 81.14), while the Or values are almost negligible (0.56–4.87, with an average of 1.00). The An values range from 12.31–24.15, with an average of 17.86. Thus, all the plagioclases of the Bure adakitic rock are macro-feldspar (Figure 4a). In the plagioclase porphyry of the Bure adakitic rock, the content of An and Al<sub>2</sub>O<sub>3</sub> has a relatively coupled synchronous change trend (Figure 5c,d). The contents of An are higher in the core and mantle, with an increasing trend from the core to the mantle, and a decreasing trend from the mantle to the edge.

#### 4.1.3. Biotite

The Fe<sup>2+</sup> and Fe<sup>3+</sup> in the biotite of the Bure adakitic rock were adjusted using the method proposed by [38], and the number of cations and related parameters of the biotite were calculated using 22 oxygen atoms as the unit. In the major element content of the Bure adakitic rock, there is 35.19–39.67 wt% of SiO<sub>2</sub>, with an average value of 37.65 wt%. The biotite has relatively high contents of FeO (16.11–20.99 wt%; average value of 19.12 wt%), Al<sub>2</sub>O<sub>3</sub> (13.96–19.13 wt%; average value of 15.77 wt%), and TiO<sub>2</sub> (2.01–3.84 wt%; average value of 2.90 wt%). In comparison, the MgO, K<sub>2</sub>O, Na<sub>2</sub>O, and CaO contents in biotite are relatively low, with values of 6.54–9.59 wt% of MgO (average value of 8.33 wt%), 7.07–9.85 wt% of K<sub>2</sub>O (average value of 8.33 wt%), 0.01–0.16 wt% of Na<sub>2</sub>O (average value of 0.08 wt%), and 0.08–0.33 wt% of CaO (average value of 0.16 wt%) (Table 3; Figure 4b).

The low Ca content of the biotite indicates that it was not, or only rarely, affected by chlorite and sericite alteration caused by primary metamorphism after the magmatic stage [39]. In addition, the Ti atomic numbers of the biotite in this study range from 0.13 to 0.22 (mean of 0.17), which is consistent with the fact that the Ti atomic number in the magmatic biotite is less than 0.55. The Fe<sup>2+</sup>/(Mg + Fe<sup>2+</sup>) ratio in the biotite presents a small variation (0.26–0.52, with an average value of 0.38), also suggesting that the biotite is of magmatic origin. The FeO, MgO, and K<sub>2</sub>O contents from the core to the edge of the biotite fluctuate slightly, showing a gentle trend and indicating that there was no mixing of basic magmatic components during crystallization (Figure 5e,f). Generally, the substitution modes of Mg<sup>2+</sup> and Al<sup>3+</sup> are crucial in calc-alkaline and peraluminous magmatic systems. The obvious negative correlation of MgO and Al<sub>2</sub>O<sub>3</sub> in the biotite implies that the displacement reaction of Mg<sup>2+</sup> and Al<sup>3+</sup> may have occurred during the crystallization process of the calc-alkaline and peraluminous magmatic system (Figure 6; [40]).

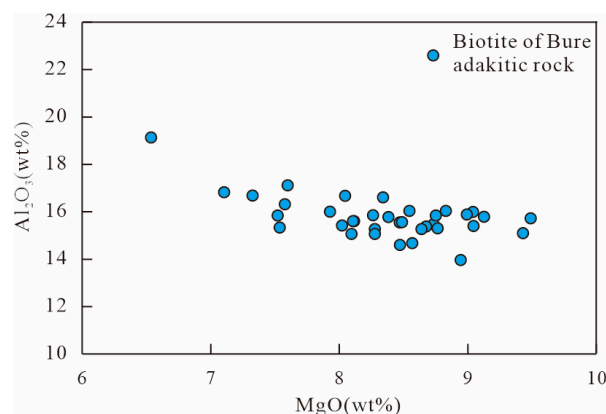


**Figure 6.** Diagram of the chemical variation of Al<sub>2</sub>O<sub>3</sub> vs. MgO in the biotite.

**Table 2.** Electron microprobe composition of plagioclase (wt%) for the Bure adakitc rock.

	Grt8-1 -fs02	Grt8-1 -fs03	Grt8-1 -fs04	Grt8-1 -fs05	Grt8-1 -fs06	Grt8-1 -fs07	Grt8-1 -fs08	Grt8-1 -fs09	Grt8-2 -fs01	Grt8-2 -fs02	Grt8-2 -fs03	Grt8-2 -fs04	Grt8-2 -fs06	Grt3-2 -fs01	Grt3-2 -fs02	Grt3-2 -fs03	Grt3-2 -fs04	Grt3-2 -fs05	Grt3-2 -fs06	Grt3-2 -fs07	Grt3-2 -fs08	
CaO	3.13	3.07	3.28	3.39	3.65	2.68	2.99	2.92	3.65	3.65	3.61	3.26	3.62	2.52	3.54	3.93	4.00	3.75	3.94	3.42	2.78	
Na <sub>2</sub> O	9.68	9.50	10.02	9.80	7.11	9.69	9.49	9.55	9.52	9.44	9.66	8.40	8.60	9.69	9.72	6.71	8.37	9.63	7.98	8.56	7.96	
K <sub>2</sub> O	0.12	0.18	0.19	0.10	0.16	0.15	0.17	0.14	0.16	0.13	0.14	0.13	0.09	0.33	0.13	0.17	0.15	0.17	0.18	0.13	0.74	
SrO																						
TFeO																						
MgO																						
SiO <sub>2</sub>	64.99	64.61	65.70	64.23	65.06	65.05	65.12	64.05	64.36	64.72	64.10	65.01	65.56	64.62	65.70	66.41	66.00	65.07	66.07	65.81	64.70	
MnO																						
Al <sub>2</sub> O <sub>3</sub>	22.68	22.89	23.32	23.55	24.11	22.59	23.24	22.46	23.25	23.66	22.67	23.58	24.13	21.95	23.07	23.74	23.50	23.11	22.97	23.41	23.11	
BaO																						
Total	100.59	100.25	102.52	101.07	100.10	100.16	101.00	99.13	100.94	101.62	100.17	100.38	102.01	99.10	102.15	100.95	102.01	101.72	101.13	101.33	99.29	
	Number of cation on basis of 8 oxygens																					
Si	5.686	5.671	5.652	5.607	5.668	5.706	5.668	5.684	5.625	5.615	5.648	5.671	5.638	5.733	5.668	5.725	5.676	5.645	5.720	5.690	5.706	
Al	1.754	1.776	1.774	1.817	1.857	1.752	1.788	1.762	1.796	1.815	1.765	1.818	1.834	1.722	1.759	1.809	1.787	1.772	1.758	1.789	1.802	
Mg	0.000	0.000	0.000	0.000	0.000	0.000	0.000	0.000	0.000	0.000	0.000	0.000	0.000	0.000	0.000	0.000	0.000	0.000	0.000	0.000	0.000	
Fe	0.000	0.000	0.000	0.000	0.000	0.000	0.000	0.000	0.000	0.000	0.000	0.000	0.000	0.000	0.000	0.000	0.000	0.000	0.000	0.000	0.000	
Mn	0.000	0.000	0.000	0.000	0.000	0.000	0.000	0.000	0.000	0.000	0.000	0.000	0.000	0.000	0.000	0.000	0.000	0.000	0.000	0.000	0.000	
Ca	0.147	0.144	0.151	0.158	0.170	0.126	0.139	0.139	0.171	0.170	0.170	0.152	0.167	0.120	0.163	0.181	0.184	0.174	0.182	0.159	0.132	
Na	0.410	0.404	0.418	0.415	0.300	0.412	0.400	0.411	0.403	0.397	0.412	0.355	0.358	0.417	0.406	0.280	0.349	0.405	0.335	0.359	0.340	
K	0.003	0.005	0.005	0.003	0.005	0.004	0.005	0.004	0.004	0.004	0.004	0.004	0.003	0.009	0.003	0.005	0.004	0.005	0.005	0.003	0.021	
Sr	0.000	0.000	0.000	0.000	0.000	0.000	0.000	0.000	0.000	0.000	0.000	0.000	0.000	0.000	0.000	0.000	0.000	0.000	0.000	0.000	0.000	
Ba	0.000	0.000	0.000	0.000	0.000	0.000	0.000	0.000	0.000	0.000	0.000	0.000	0.000	0.000	0.000	0.000	0.000	0.000	0.000	0.000	0.000	
An	15.0	15.0	15.2	15.9	21.9	13.1	14.7	14.3	17.5	17.5	17.0	17.5	18.8	12.3	16.6	24.1	20.7	17.5	21.2	18.0	15.4	
Ab	84.2	84.0	83.8	83.5	77.0	86.0	84.3	84.8	81.8	81.8	82.3	81.6	80.6	85.8	82.7	74.6	78.4	81.5	77.7	81.3	79.7	
Or	0.7	1.0	1.0	0.6	1.2	0.9	1.0	0.8	0.9	0.8	0.8	0.9	0.6	1.9	0.7	1.2	0.9	0.9	1.1	0.8	4.9	
	Grt3-3 -fs01	Grt3-3 -fs02	Grt3-3 -fs03	Grt3-3 -fs04	Grt3-6 -fs01	Grt3-6 -fs02	Grt3-6 -fs03	Grt3-6 -fs04	Grt3-6 -fs06	Grt3-8 -fs01	Grt3-8 -fs02	Grt3-8 -fs03	Grt3-8 -fs04	Grt3-8 -fs05	Grt3-8 -fs06	Grt3-8 -fs07						
CaO	3.58	3.54	3.33	3.17	3.69	3.52	3.60	3.62	3.59	4.00	3.79	3.88	4.28	3.97	3.87	3.91						
Na <sub>2</sub> O	8.47	7.73	8.91	9.19	8.83	9.85	7.93	8.26	8.90	8.16	8.89	7.54	9.31	8.90	8.83	9.52						
K <sub>2</sub> O	0.15	0.12	0.12	0.12	0.18	0.10	0.14	0.16	0.13	0.18	0.16	0.18	0.15	0.12	0.16	0.20						
SrO																						
TFeO																						
MgO																						
SiO <sub>2</sub>	66.55	66.89	67.75	66.29	65.18	64.62	65.97	65.88	66.04	65.32	64.39	65.27	63.68	63.52	63.94	63.39						
MnO																						
Al <sub>2</sub> O <sub>3</sub>	23.09	23.42	22.32	22.36	22.92	23.03	23.15	23.14	23.20	23.31	23.22	23.57	23.63	23.21	23.13	23.37						
BaO																						
Total	101.84	101.70	102.42	101.14	100.79	101.12	100.78	101.07	101.84	100.97	100.46	100.44	101.05	99.72	99.92	100.39						
	Number of cation on basis of 8 oxygens																					
Si	5.723	5.737	5.789	5.749	5.683	5.639	5.721	5.708	5.692	5.675	5.642	5.682	5.573	5.614	5.634	5.584						
Al	1.755	1.776	1.686	1.714	1.766	1.777	1.774	1.772	1.768	1.790	1.798	1.814	1.828	1.814	1.802	1.820						
Mg	0.000	0.000	0.000	0.000	0.000	0.000	0.000	0.000	0.000	0.000	0.000	0.000	0.000	0.000	0.000	0.000						
Fe	0.000	0.000	0.000	0.000	0.000	0.000	0.000	0.000	0.000	0.000	0.000	0.000	0.000	0.000	0.000	0.000						
Mn	0.000	0.000	0.000	0.000	0.000	0.000	0.000	0.000	0.000	0.000	0.000	0.000	0.000	0.000	0.000	0.000						
Ca	0.165	0.162	0.152	0.147	0.172	0.164	0.167	0.168	0.166	0.186	0.178	0.181	0.200	0.188	0.182	0.185						
Na	0.353	0.321	0.369	0.386	0.373	0.417	0.333	0.347	0.372	0.344	0.378	0.318	0.395	0.381	0.377	0.406						
K	0.004	0.003	0.003	0.003	0.005	0.003	0.004	0.005	0.003	0.005	0.004	0.005	0.004	0.003	0.004	0.005						
Sr	0.000	0.000	0.000	0.000	0.000	0.000	0.000	0.000	0.000	0.000	0.000	0.000	0.000	0.000	0.000	0.000						
Ba	0.000	0.000	0.000	0.000	0.000	0.000	0.000	0.000	0.000	0.000	0.000	0.000	0.000	0.000	0.000	0.000						
An	18.8	20.0	17.0	15.9	18.6	16.4	19.9	19.3	18.1	21.1	18.9	21.9	20.1	19.7	19.3	18.3						
Ab	80.3	79.2	82.3	83.4	80.4	83.1	79.2	79.7	81.2	77.8	80.2	77.0	79.1	79.7	79.8	80.6						
Or	0.9	0.8	0.8	0.7	1.1	0.6	0.9	1.0	0.8	1.1	0.9	1.2	0.8	0.7	0.9	1.1						

Note: Blank space is below the detection limit.

**Table 3.** Electron microprobe composition of biotite (wt%) for the Bure adakitic rock.

	Grt3-1 -ms01	Grt3-1 -ms02	Grt3-1 -ms03	Grt3-1 -ms04	Grt3-1 -ms05	Grt3-1 -ms06	Grt3-1 -ms07	Grt3-3 -ms01	Grt3-3 -ms02	Grt3-3 -ms04	Grt3-3 -ms06	Grt3-3 -ms07	Grt3-3 -ms08	Grt3-3 -ms09	Grt3-3 -ms10	Grt3-3 -ms11	Grt3-3 -ms12	Grt3-3 -ms13	Grt3-6 -ms01	Grt3-6 -ms02	Grt3-6 -ms03	Grt3-6 -ms04
SiO <sub>2</sub>	37.512	36.417	37.188	36.342	37.424	37.667	36.166	36.344	38.646	37.178	37.884	37.184	38.548	35.189	37.295	36.984	35.891	37.385	38.104	38.663	37.11	37.509
TiO <sub>2</sub>	2.547	2.994	2.657	2.731	2.663	2.574	2.866	2.399	2.314	2.645	3.06	3.024	2.596	2.058	2.673	2.73	2.919	2.736	3.586	3.817	3.479	3.536
Al <sub>2</sub> O <sub>3</sub>	15.299	15.548	15.843	15.789	13.959	15.272	15.474	15.725	15.99	15.1	15.565	15.06	16.669	19.128	16.605	15.403	14.672	15.376	16.037	15.856	15.883	16.038
FeO	20.427	19.903	19.169	20.682	20.507	19.56	20.307	20.457	18.94	18.25	19.449	20.196	18.327	16.111	19.864	20.587	19.835	20.987	19.921	18.693	20.427	19.627
MnO	0.226	0.218	0.214	0.213	0.28	0.222	0.252	0.224	0.233	0.19	0.251	0.267	0.218	0.181	0.27	0.249	0.283	0.262	0.252	0.211	0.198	0.162
MgO	8.765	8.47	8.752	9.126	8.945	8.639	8.734	9.49	9.04	9.43	8.488	8.277	8.045	6.535	8.341	9.045	8.568	8.675	8.546	8.675	8.993	8.829
CaO	0.118	0.18	0.182	0.143	0.139	0.265	0.1	0.193	0.31	0.332	0.129	0.316	0.273	0.18	0.082	0.142	0.29	0.202	0.276	0.081	0.135	0.081
Na <sub>2</sub> O	0.097	0.054	0.085	0.096	0.089	0.065	0.089	0.065	0.078	0.089	0.095	0.081	0.108	0.033	0.076	0.11	0.159	0.121	0.104	0.073	0.078	0.078
K <sub>2</sub> O	9.25	9.239	8.879	9.583	9.627	8.713	9.516	9.699	9.025	8.992	9.404	9.195	8.297	7.696	9.059	9.231	8.835	9.448	9.141	9.302	9.852	9.425
Total	94.241	93.023	92.969	94.705	93.633	92.977	93.504	94.596	94.576	92.206	94.325	93.6	93.081	87.111	94.265	94.481	91.452	95.192	95.967	94.958	96.155	95.285
Number of cation on basis of 22 oxygens																						
Si	2.833	3.458	2.898	2.853	2.889	2.812	2.927	2.927	2.832	2.815	2.937	2.907	2.909	2.895	2.952	2.851	2.865	2.858	2.865	2.873	2.875	2.927
Al <sup>IV</sup>	1.167	0.542	1.102	1.147	1.111	1.188	1.073	1.073	1.168	1.185	1.063	1.093	1.091	1.105	1.048	1.149	1.135	1.142	1.135	1.127	1.125	1.073
Al <sup>VI</sup>	0.028	1.648	0.292	0.288	0.340	0.252	0.214	0.326	0.260	0.251	0.370	0.298	0.318	0.277	0.456	0.677	0.369	0.260	0.245	0.266	0.301	0.341
Ti	0.129	0.000	0.148	0.176	0.155	0.159	0.157	0.151	0.169	0.140	0.132	0.156	0.177	0.177	0.150	0.125	0.154	0.159	0.175	0.158	0.204	0.217
Fe <sup>3+</sup>	0.129	0.124	0.280	0.281	0.323	0.211	0.240	0.341	0.233	0.189	0.343	0.303	0.322	0.300	0.440	0.489	0.322	0.254	0.268	0.255	0.344	0.397
Fe <sup>2+</sup>	0.638	0.000	1.040	1.023	0.922	1.127	1.101	0.931	1.097	1.136	0.861	0.890	0.927	1.015	0.734	0.603	0.954	1.076	1.056	1.093	0.913	0.787
Mn	0.003	0.000	0.015	0.014	0.014	0.014	0.019	0.015	0.017	0.015	0.015	0.013	0.016	0.018	0.014	0.012	0.018	0.016	0.019	0.017	0.016	0.014
Mg	1.841	0.211	1.010	0.989	1.014	1.053	1.043	1.001	1.020	1.096	1.024	1.099	0.972	0.961	0.918	0.789	0.955	1.042	1.020	0.994	0.961	0.932
Ca	0.025	0.000	0.010	0.015	0.015	0.012	0.012	0.008	0.016	0.025	0.028	0.028	0.011	0.026	0.022	0.016	0.007	0.012	0.025	0.017	0.022	0.007
Na	0.032	0.039	0.015	0.008	0.013	0.014	0.013	0.010	0.014	0.010	0.011	0.013	0.014	0.012	0.016	0.005	0.011	0.016	0.025	0.018	0.015	0.011
K	0.913	0.888	0.912	0.923	0.880	0.946	0.961	0.864	0.951	0.959	0.875	0.897	0.921	0.913	0.810	0.795	0.888	0.910	0.900	0.926	0.880	0.898
	Grt8-1 -ms01	Grt8-1 -ms02	Grt8-1 -ms03	Grt8-1 -ms04	Grt8-1 -ms05	Grt8-1 -ms06	Grt8-1 -ms07	Grt8-1 -ms08	Grt8-3 -ms01	Grt8-3 -ms02	Grt8-3 -ms03	Grt8-3 -ms04	Grt8-3 -ms05	Grt8-3 -ms06	Grt8-5 -ms01	Grt8-5 -ms02	Grt8-5 -ms03	Grt8-5 -ms04	Grt8-5 -ms05	Grt8-5 -ms06	Grt8-5 -ms07	Grt8-5 -ms08
SiO <sub>2</sub>	46.568	47.913	45.736	46.328	45.586	46.436	47.622	47.476	36.007	37.312	38.717	39.669	38.79	39.312	38.683	37.77	37.651	39.147	38.832	38.474	38.011	38.31
TiO <sub>2</sub>	1.106	1.021	1.089	0.988	1.444	0.712	0.435	0.41	2.567	2.603	2.652	2.43	2.555	2.708	2.49	3.608	2.887	3.377	3.615	2.806	3.821	3.836
Al <sub>2</sub> O <sub>3</sub>	29.682	29.113	29.725	29.342	29.037	29.447	30.081	30.942	14.599	15.062	15.274	16.682	15.338	16.827	17.12	15.606	15.604	15.778	15.419	16	16.315	15.844
FeO	4.451	5.048	4.95	5.009	4.875	5.623	5.254	5.515	18.37	18.689	18.977	17.017	17.374	17.353	18.587	19.489	20.461	17.878	18.553	17.535	17.189	18.617
MnO	0.046	0.016	0.072	0.036	0.038	0.048	0.019	0.064	0.299	0.314	0.234	0.228	0.305	0.223	0.301	0.306	0.283	0.266	0.287	0.236	0.2	0.217
MgO	1.586	1.746	1.411	1.418	1.519	1.659	1.582	1.662	8.473	8.096	8.276	7.325	7.537	7.104	7.598	8.116	8.108	8.382	8.021	7.928	7.576	7.522
CaO	0.005	0.008	0.023	0.019				0.005	0.128	0.13	0.081	0.105	0.076	0.133	0.118	0.086	0.168	0.096	0.123	0.102	0.134	0.141
Na <sub>2</sub> O	0.189	0.13	0.173	0.171	0.168	0.145	0.083	0.121	0.088	0.082	0.079	0.061	0.054	0.042	0.056	0.04	0.07	0.082	0.072	0.053	0.014	0.139
K <sub>2</sub> O	11.513	11.665	11.654	11.521	11.346	11.47	11.491	11.355	8.591	9.037	8.939	8.219	8.931	7.072	8.933	9.389	9.161	9.474	8.885	8.665	8.48	9.057
Total	95.146	96.66	94.833	94.832	94.013	95.54	96.567	97.55	89.122	91.325	93.229	91.736	90.96	90.774	93.886	94.41	94.393	94.48	93.807	91.799	91.74	93.683
Number of cation on basis of 22 oxygens																						
Si	3.183	3.229	3.152	3.187	3.165	3.179	3.209	3.169	2.920	2.950	2.985	3.046	3.039	3.036	2.947	2.899	2.901	2.966	2.967	2.984	2.944	2.938
Al <sup>IV</sup>	0.817	0.771	0.848	0.813	0.835	0.821	0.791	0.831	1.080	1.050	1.015	0.954	0.961	0.964	1.053	1.101	1.099	1.034	1.033	1.016	1.056	1.062
Al <sup>VI</sup>	1.574	1.541	1.567	1.567	1.540	1.555	1.597	1.604	0.316	0.354	0.372	0.556	0.456	0.568	0.484	0.310	0.318	0.375	0.356	0.447	0.433	0.370
Ti	0.057	0.052	0.056	0.051	0.075	0.037	0.022	0.021	0.157	0.155	0.154	0.140	0.151	0.157	0.143	0.208	0.167	0.193	0.208	0.164	0.223	0.221
Fe <sup>3+</sup>	0.254	0.284	0.285	0.288	0.283	0.322	0.296	0.308	0.323	0.345	0.387	0.534	0.448	0.608	0.420	0.350	0.321	0.399	0.431	0.446	0.491	0.422
Fe <sup>2+</sup>	0.000	0.000	0.000	0.000	0.000	0.000	0.000	0.000	0.923	0.891	0.837	0.558	0.691	0.513	0.764	0.901	0.997	0.733	0.755	0.691	0.622	0.772
Mn	0.003	0.001	0.004	0.002	0.002	0.003	0.001	0.004	0.021	0.021	0.015	0.015	0.020	0.015	0.019	0.020	0.018	0.017	0.019	0.016	0.013	0.014
Mg	0.162	0.175	0.145	0.145	0.157	0.169	0.159	0.165	1.024	0.954	0.951	0.839	0.880	0.818	0.863	0.929	0.931	0.947	0.914	0.917	0.875	0.860
Ca	0.000	0.001	0.002	0.001	0.000	0.000	0.000	0.000	0.011	0.011	0.007	0.009	0.006	0.011	0.010	0.007	0.014	0.008	0.010	0.008	0.011	0.012
Na	0.025	0.017	0.023	0.023	0.023	0.019	0.011	0.016	0.014	0.013	0.012	0.009	0.008	0.006	0.008	0.010	0.012	0.011	0.008	0.002	0.021	0.021
K	1.004	1.003	1.025	1.011	1.005	1.002	0.988	0.967	0.889	0.912	0.879	0.805	0.893	0.697	0.868	0.919	0.900	0.916	0.866	0.857	0.838	0.886

Note: Blank space is below the detection limit.

### 4.2. Trace Element Compositions of Zircon

The zircon trace elements and calculated oxygen fugacity parameters from the Bure adakitic rock are shown in Table 4, respectively. They are depleted in LREEs and enriched in HREEs, with significant positive Ce anomalies and weak negative Eu anomalies in the chondrite-normalized REE patterns (Figure 7), indicating that they are magmatic zircons [41]. The magmatic crystallization temperatures of the Bure adakitic rock calculated based on Ti-in-zircon thermometry [42] vary from 659 to 814 °C (mean of 705 °C). The corresponding  $\log fO_2$  values of the zircons from the Bure adakitic rock range from  $-11.5$  to  $-5.2$ , with a median of  $-8.6$  [43–45].

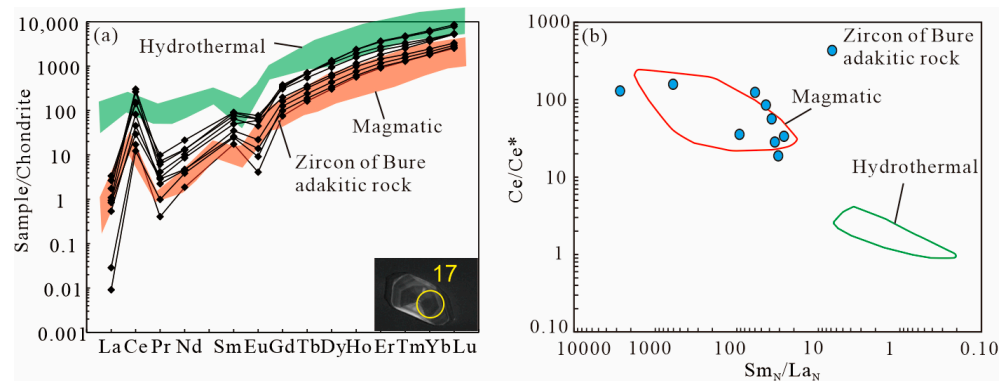


**Figure 7.** Chondrite-normalized REE patterns (a) and  $Ce/Ce^*$  vs.  $Sm_N/La_N$  (b); [41]. The Chondrite data for the normalization and plotting are from [46].

**Table 4.** Trace element compositions of zircon (ppm) for the Bure adakitic rock.

No.	La	Ce	Pr	Nd	Sm	Eu	Gd	Tb	Dy	Ho	Er	Tm	Yb	Lu	Y	Ti	$t^\circ C$ [42]	$(Ce/Ce^*)_D$ [43]	$\log fO_2$ [45]	$\Delta FMQ$ [45]
BR0101 Grt1-05	0.01	10.39	0.04	0.87	2.66	0.24	15.51	6.08	77.30	32.03	150.74	32.78	307.81	63.94	957.16	4.49	675.1	383.1	-9.6	7.9
BR0101 Grt1-06	0.22	49.94	0.21	2.13	5.36	1.27	32.86	11.94	146.11	55.28	240.64	46.74	413.50	84.28	1513.41	3.63	659.0	560.7	-9.1	8.9
BR0101 Grt1-07	0.13	27.75	0.29	3.99	7.62	3.49	40.70	13.41	163.41	64.89	299.34	64.48	615.10	132.45	1890.88	21.77	814.2	190.1	-5.2	9.0
BR0101 Grt1-15	0.63	88.37	0.94	10.03	13.87	4.47	62.97	20.56	239.48	89.35	382.39	74.31	658.28	135.13	2380.80	8.13	723.0	177.5	-9.8	6.4
BR0101 Grt1-17	0.26	161.18	0.39	4.73	9.97	2.61	71.27	26.37	336.42	132.64	588.23	115.67	1005.19	199.90	3637.32	3.06	646.3	971.1	-7.8	10.5
BR0101 Grt1-26	0.41	184.47	0.69	6.19	11.69	3.74	66.89	25.61	325.23	134.75	609.07	121.47	1079.09	217.81	3838.12	5.38	689.1	874.7	-5.7	11.5
BR0101 Grt1-32	0.20	17.83	0.27	2.20	3.99	0.80	20.21	7.06	86.07	34.79	161.39	33.70	315.24	68.03	1017.32	8.03	721.8	224.5	-9.0	7.3
BR0101 Grt1-35	0.00	7.49	0.09	1.79	3.76	0.53	25.91	8.91	110.30	42.79	192.76	39.88	359.63	74.73	1224.30	7.90	720.5	116.6	-11.5	4.8
BR0101 Grt1-39	0.80	93.02	0.58	6.05	13.51	3.77	77.29	26.39	298.01	108.37	448.54	84.63	703.25	137.54	2797.50	5.60	692.3	284.1	-9.7	7.3

### 4.3. Zircon Lu-Hf Isotopes and Whole-Rock Sr-Nd Isotopes

Ten Lu-Hf isotopic analyses were conducted on the zircons of the Bure adakitic rock sample, yielding  $^{176}Hf/^{177}Hf$  ratios of 0.282572–0.282734, and  $\epsilon_{Hf}(t)$  values from 7.64 to 12.99 (average value = 11; Table 5). On the Age- $\epsilon_{Hf}(t)$  diagram, the corresponding two-stage Hf model ages vary from 802–1161 Ma (Figure 8a). The Sr-Nd isotopic results of the Bure adakitic rock are shown in Table 6. The  $^{87}Sr/^{86}Sr$  ratios ranging from 0.707381 to 0.70745 (average value = 0.70741) are higher than that of the current original mantle value ( $^{87}Sr/^{86}Sr = 0.7045$ ; Table 6). Correspondingly, the calculated ( $^{87}Sr/^{86}Sr$ )<sub>i</sub> ratios vary from 0.70088 to 0.70275 (average value = 0.70184), and the  $\epsilon_{Nd}(t)$  values have a relatively large variation of 3.26 to 7.28 (average value = 4.72; Figure 8b). Their two-stage Nd model ages range from 820 to 1210 Ma.

**Table 5.** Zircon Hf isotopic data for the Bure adakitic rock.

No.	$^{176}\text{Hf}/^{177}\text{Hf}$	1 $\sigma$	$^{176}\text{Lu}/^{177}\text{Hf}$	1 $\sigma$	$^{176}\text{Yb}/^{177}\text{Hf}$	1 $\sigma$	Age (Ma) [7]	$\epsilon_{\text{Hf}}(\text{t})$ [47]	TDM <sub>2</sub> (Ma)
BR0101Grt1-02	0.282734	0.000020	0.001766	0.000051	0.064510	0.001820	660	12.44	803
BR0101Grt1-05	0.282623	0.000013	0.000892	0.000018	0.029611	0.000544	753	10.91	974
BR0101Grt1-07	0.282680	0.000021	0.001743	0.000019	0.055813	0.000457	743	12.29	877
BR0101Grt1-12	0.282702	0.000017	0.002429	0.000022	0.070191	0.000389	743	12.73	849
BR0101Grt1-17	0.282599	0.000020	0.003626	0.000051	0.129672	0.002161	744	8.50	1122
BR0101Grt1-21	0.282689	0.000022	0.002049	0.000063	0.067411	0.002036	696	11.48	893
BR0101Grt1-26	0.282718	0.000021	0.003151	0.000071	0.109087	0.002564	746	12.99	834
BR0101GRT1-10	0.282631	0.000019	0.002470	0.000074	0.056882	0.001625	715	9.63	1027
BR0101GRT1-15	0.282645	0.000020	0.002279	0.000038	0.060088	0.001038	728	10.46	983
BR0101GRT1-22	0.282667	0.000017	0.000706	0.000009	0.017882	0.000247	729	12.02	883
BR0101GRT1-28	0.282657	0.000022	0.001282	0.000020	0.033778	0.000571	735	11.54	919
BR0101GRT1-31	0.282644	0.000021	0.001278	0.000002	0.034658	0.000082	713	10.61	962
BR0101GRT1-32	0.282620	0.000023	0.000766	0.000016	0.020989	0.000557	731	10.38	991
BR0101GRT1-35	0.282644	0.000020	0.001313	0.000004	0.033838	0.000049	753	11.44	940
BR0101GRT1-39	0.282572	0.000029	0.002650	0.000025	0.072997	0.000613	724	7.64	1161

**Table 6.** Sr–Nd isotopic data for the Bure adakitic rock.

Sample No.	$^{87}\text{Rb}/^{86}\text{Sr}$	$^{87}\text{Sr}/^{86}\text{Sr}$	$\pm 2\sigma$	$(^{87}\text{Sr}/^{86}\text{Sr})_i$	$^{147}\text{Sm}/^{144}\text{Nd}$	$^{143}\text{Nd}/^{144}\text{Nd}$	$\pm 2\sigma$	$\epsilon_{\text{Nd}}(\text{t})$	TDM <sub>2</sub> (Ma)
BR0101Grt1	0.523	0.707381	0.000006	0.701898	0.122	0.512463	0.000009	3.62	1140
BR0101Grt2	0.623	0.707409	0.000006	0.700880	0.115	0.512618	0.000007	7.28	820
BR0101Grt3	0.449	0.707450	0.000010	0.702746	0.130	0.512485	0.000007	3.26	1210

Note:  $\epsilon_{\text{Nd}}(\text{t}) = [({}^{143}\text{Nd}/{}^{144}\text{Nd})_{\text{sample}}(\text{t}) / ({}^{143}\text{Nd}/{}^{144}\text{Nd})_{\text{CHUR}}(\text{t}) - 1] \times 10^{-4}$ ;  $\text{TDM}_2 = 1/\lambda \times [1 + ({}^{143}\text{Nd}/{}^{144}\text{Nd})_{\text{sample}} - ({}^{147}\text{Sm}/{}^{144}\text{Nd})_{\text{sample}} - ({}^{147}\text{Sm}/{}^{144}\text{Nd})_{\text{crust}}] \times (e^{\lambda t} - 1) - ({}^{143}\text{Nd}/{}^{144}\text{Nd})_{\text{DM}} / (({}^{147}\text{Sm}/{}^{144}\text{Nd})_{\text{crust}} - ({}^{147}\text{Sm}/{}^{144}\text{Nd})_{\text{DM}})$ .  $({}^{147}\text{Sm}/{}^{144}\text{Nd})_{\text{CHUR}} = 0.1967$ , and  $({}^{143}\text{Nd}/{}^{144}\text{Nd})_{\text{CHUR}} = 0.512638$  [48];  $({}^{147}\text{Sm}/{}^{144}\text{Nd})_{\text{DM}} = 0.2136$ , and  $({}^{143}\text{Nd}/{}^{144}\text{Nd})_{\text{DM}} = 0.51315$  [49];  $({}^{147}\text{Sm}/{}^{144}\text{Nd})_{\text{crust}} = 0.118$  [50].

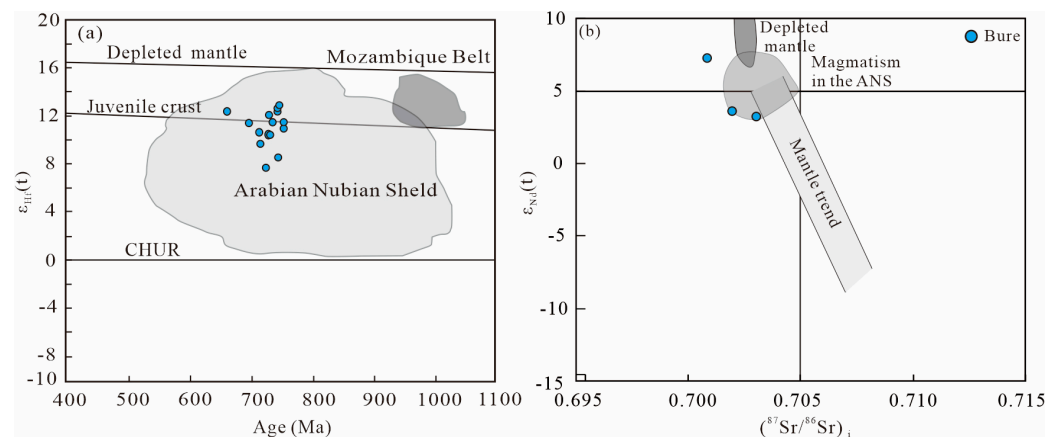


**Figure 8.** Diagrams of Hf (a) and Sr–Nd isotopes (b) for the Bure adakitic rock. Zircon Hf isotope-age data obtained from the Arabian Nubian Shield [51]; Mozambique Belt [52]; ranges for depleted mantle (DM), chondritic uniform reservoir (CHUR), and juvenile crust from Griffin et al. [53]. Sr–Nd isotopic data of the Depleted Mantle [54] and the Arabian Nubian Shield [10,28,55].

## 5. Discussion

### 5.1. Physicochemical Condition of Magma Crystallization

Zircon, a mineral that typically crystallizes early in acidic magma, usually at temperatures close to the magma formation temperature, serves as an indicator of initial crystallization in granitoids. Thus, the magmatic crystallization temperature of the Bure

adakitic rock calculated based on Ti-in-zircon thermometry varies from 659 to 814 °C, with a mean of 705 °C. In conclusion, we propose that the crystallization temperature of the Bure adakitic rock was concentrated between 659 to 814 °C.

Emplacement pressure can be estimated from biotite compositions using the empirical formula of the biotite all-aluminum manometer in granitoids based on the hornblende manometer:  $p \times 100 = 3.03 \times T^{Al} - 6.53 (\pm 0.33)$  [56]. The estimated pressures show a range from  $1.75 \times 10^5$  to  $2.81 \times 10^5$  Pa (mean  $2.09 \times 10^5$  Pa) for the Bure adakitic rock. The calculated emplacement depth of the Bure adakitic rock is 6.39~10.2 km (mean 7.60 km) according to the empirical formula  $p = \rho gh$  ( $\rho = 2800 \text{ kg/m}^3$ ;  $g = 9.8 \text{ m/s}^2$ ), which indicates that the magmatic emplacement depth was relatively deep.

Generally, the  $\text{Fe}^{3+}$ ,  $\text{Fe}^{2+}$ , and  $\text{Mg}^{2+}$  values in biotite can be used to estimate the oxygen fugacity during crystallization. The electron probe data of the biotite in the Bure adakitic rock projected into the correlation diagram of biotite composition and oxygen buffer pairs show that all the data fall between the Ni-NiO and  $\text{Fe}_2\text{O}_3\text{-Fe}_3\text{O}_4$  buffer lines and all are close to the Ni-NiO buffer lines, implying that the biotite in the Bure adakitic rock crystallized in a high oxygen fugacity environment (Figure 9). The presence of the variable valence elements of Ce and Eu in zircon makes it an ideal candidate for calculating the oxygen fugacity in coexisting magmas [42]. Unlike most rare earth elements, which exist in the +3 valence, the Ce element can exist in the form of  $\text{Ce}^{4+}$  in magmas. The similar radius of  $\text{Ce}^{4+}$  and  $\text{Zr}^{4+}$  leads to  $\text{Ce}^{4+}$  being more likely than  $\text{Ce}^{3+}$  to enter the zircon lattice due to isomorphism. Thus, Ballard et al. [43] proposed that the positive Ce anomaly of zircon can reflect the oxidation state in magma. Most of the points of the Bure adakitic rock are in the FMQ–HM range, and nearly half of the calculated zircon points reach the magmatic oxygen fugacity level of MH, suggesting a high oxygen fugacity of the magma (Figure 10a,b).

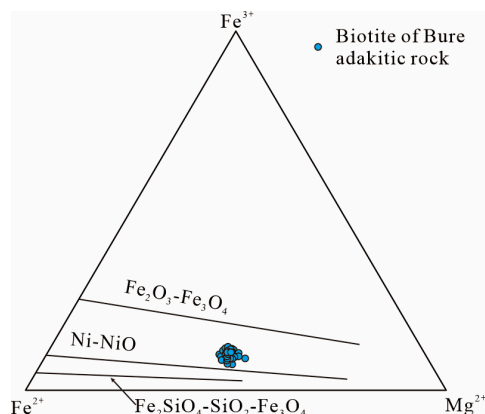


Figure 9. Correlative diagram between biotite composition and oxygen buffer-reagents [57].

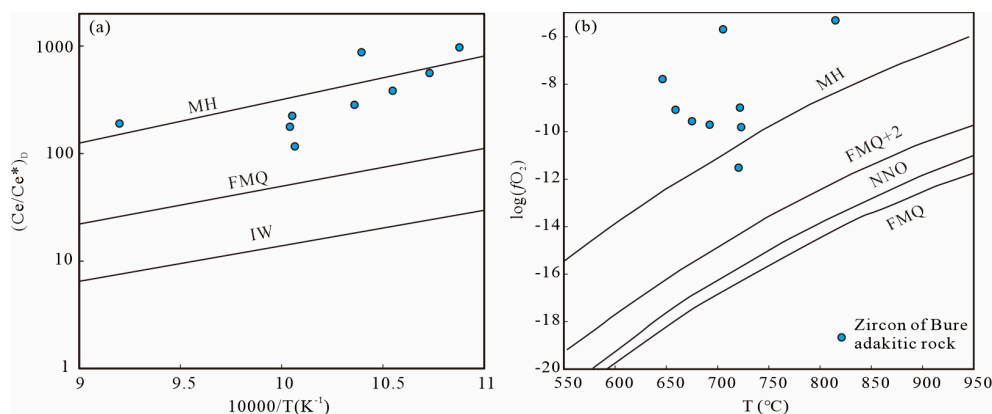
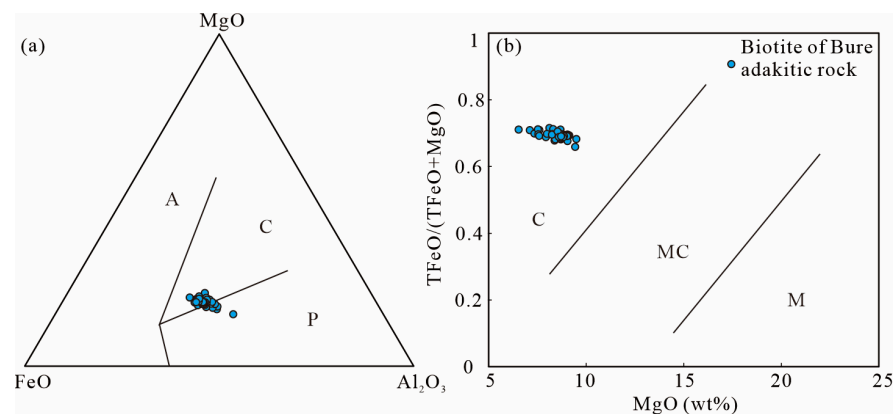


Figure 10.  $(\text{Ce}/\text{Ce}^*)_D$  of the zircons vs.  $10,000/T$  (a); [58]) and  $\log f\text{O}_2$  vs.  $T$  (b); [59]) diagrams for the Bure adakitic rock.

### 5.2. Magma Source and Genesis

The relationship between the MB and ANS, collectively referred to as the EAO by Stern [4], is not well understood. The inherited zircons of Mesoproterozoic age reported from the different granitic populations in the contrasting low- and high-grade terranes by Kebede et al. [8,9] indicate a contribution of pre-Neoproterozoic crustal material to the source magmas of these rocks. In eastern Ethiopia, Teklay et al. [60] suggested pre-Neoproterozoic crustal reworking based on Paleoproterozoic zircon inheritance and Mesoproterozoic to Archean crust residence ages for the granitoids. Kröner and Sassi [61] also reported a Mesoproterozoic to Paleoproterozoic crystalline basement intruded by Neoproterozoic granitoids in northern Somalia. Farther north in the ANS, studies [62–64] rule out the involvement of pre-Neoproterozoic crust. These studies seem to indicate the increasing importance of pre-Neoproterozoic crust southwards in the EAO, but detailed and systematic investigations are necessary to fully understand the issue.

As mentioned above, the biotite in the Bure adakitic rock enriched in iron and aluminum [7], together with the major elements plotted onto the MgO–FeO–Al<sub>2</sub>O<sub>3</sub> and TFeO/(TFeO + MgO)–MgO diagrams, suggest that the rock is a calc-alkaline orogenic granite (Figure 11a), with a crustal magmatic source affinity (Figure 11b). The positive  $\epsilon_{\text{Hf}}(t)$  values > 7 (ranging from 7.64 to 12.99) of the Bure adakitic rock fall above the Hf isotope evolution line of the chondrites, and completely fall into the ANS area [51], implying generation from a juvenile source. The Sr–Nd isotope results show that the Bure adakitic rock has low ( $^{87}\text{Sr}/^{86}\text{Sr}$ )<sub>i</sub> values of 0.70088–0.70275 and positive  $\epsilon_{\text{Nd}}(t)$  values of 3.26 to 7.28, suggesting that the rock was sourced from a juvenile crust rather than lithospheric mantle material [54]. The ( $^{87}\text{Sr}/^{86}\text{Sr}$ )<sub>i</sub>– $\epsilon_{\text{Nd}}(t)$  map shows that the Bure adakitic rock is consistent with the magmatic rocks in the ANS [10,28,55], which further indicates that the magma was derived from a juvenile crust. Although the Nd isotope depleted mantle model age of 820 Ma to 1210 Ma (average age = 1060 Ma) of the Bure adakitic rock is older than that of the crystallization age of 733.8 Ma [7], it is obviously younger than the Mesoproterozoic and Archaean ancient crust. This result further demonstrates that the Arab-Nubian Shield in the Neoproterozoic was characterized by a juvenile crust. The mean Nd model age for the WES is 1.03 Ga, which is between those calculated by Stern [22] based on existing Nd isotopic data from northern Ethiopia and Eritrea (mean value of 0.87 Ga; [22,55,65]) and the Southern Ethiopia Shield (1.13 Ga), respectively. This indicates that the transition between northern and southern Ethiopia lies in the Western Ethiopia Shield, reflecting a gradual transition between the northern ANS and the southern MB of the EAO. Additionally, the mean Nd model ages from the northern parts (Egypt, Sudan, Arabia Shield, and Eritrea and northern Ethiopia) to the central parts (western Ethiopia shield) and southern parts (southern Ethiopia shield, Kenya) of the EAO show an increasing trend, which indicates an increasing contribution of pre-Pan-African crust towards the southern part of the EAO (Figure 12).



**Figure 11.** MgO–FeO–Al<sub>2</sub>O<sub>3</sub> discrimination diagram of the tectonic setting (a); [66]) and TFeO/(TFeO + MgO) vs. MgO diagram (b); [67]) of biotite. A: anorogenic alkaline suites; C: calc-alkaline orogenic suites; P: peraluminous suites; C: crustal source; M: mixing source between crust and mantle; M: mantle source.

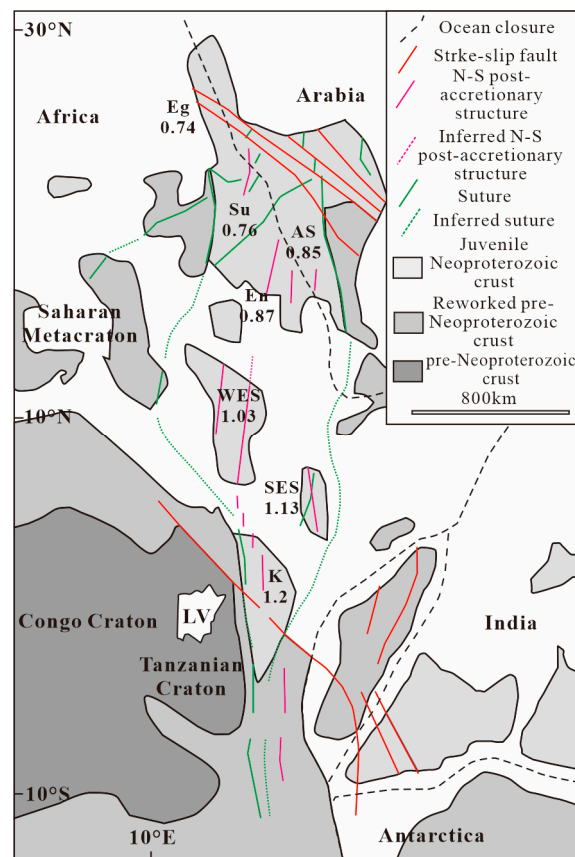


**Figure 12.** The mean Nd-model ages of the EAO in Africa [22]. Eg—Egypt; Su—Sudan; As—Arabian Shield; En—Eritrea and northern Ethiopia; SES—Southern Ethiopia Shield; K—Kenya.

### 5.3. Tectonic Environment

The plagioclase in the Bure adakitic rock shows no distinct zonal structure, indicating that the magma chamber was almost undisturbed, and the original molten slurry was in a balanced crystalline environment. In general, the crystallized minerals from the molten slurry easily reacted with the melt to form a uniform composition of minerals, leading to no zonal characteristics in the crystallized minerals. In the Lu/Hf-Y and Yb-Y diagrams of zircon, the trace elements of zircon from the Bure adakitic rock fall into the volcanic arc environment (VAB) and the area towards the within plate environment (WPB; Figure 13a,b). As mentioned above, the zircon U-Pb age of 750–710 Ma from the Bure adakitic rock [7] corresponds to the tectono-thermal event of approximately 780–700 Ma measured in previous studies of other locations in the ANS. This suggests a syn-tectonic environment [5,8–10,22]. In addition, the high SiO<sub>2</sub> (72.26–72.78 wt%), Al<sub>2</sub>O<sub>3</sub> (14.91–15.82 wt%), Sr (310–401 ppm), Sr/Y (64.9–113.6), and La/Yb (25.7–51.6), low MgO (0.27–0.41 wt%), Y (2.71–4.78 ppm), and Yb (0.20–0.31 ppm), and Na<sub>2</sub>O/K<sub>2</sub>O values of 1.13–1.38 [7] of the Bure adakitic rock suggest that it was mainly formed by the partial melting of a thickened juvenile lower crust. Consequently, we propose that the Bure adakitic rock is the product of thickened juvenile crust melting triggered by the Pan-African Orogeny during the Neoproterozoic [68].

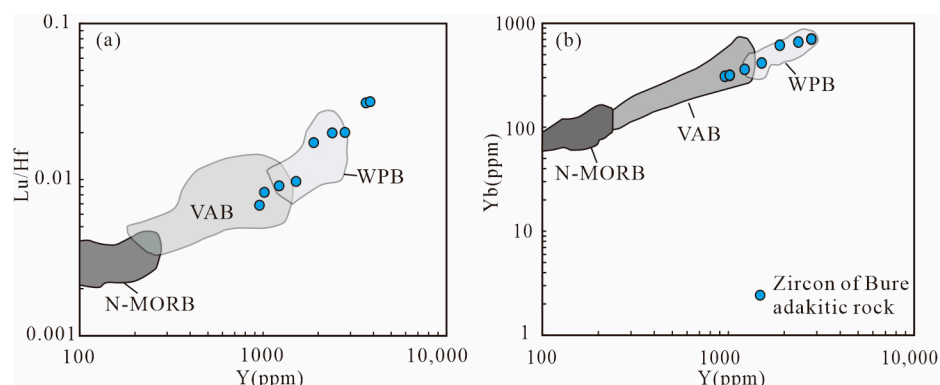


**Figure 13.** Lu/Hf vs. Y (a) and Yb vs. Y (b) diagrams of zircons [69] for the Bure adakitic rock. N-MORB: normal mid-ocean ridge basalt; VAB: volcanic arc basalt; WPB: within-plate basalt.

## 6. Conclusions

The petrological, mineralogical, and geochemical features of the Bure adakitic rock lead to the following conclusions:

- (1) The crystallization temperature of the Bure adakitic rock ranges from 659 to 814 °C, and its calculated emplacement depth was 6.39~10.2 km (average of 7.60 km). The Fe<sup>3+</sup>, Fe<sup>2+</sup>, and Mg<sup>2+</sup> values of biotite, and the positive Ce anomaly and calculated magmatic oxygen fugacity values of zircon reveal a high oxygen fugacity of the magma.
- (2) The major elements of biotite and the Sr-Nd-Hf isotopes indicate that the Bure adakitic rock was derived from juvenile crustal materials. Additionally, the mean Nd model ages progressively increase from the northern to the central and southern parts of the EAO, which indicates an increasing contribution of the pre-Pan-African crust towards the southern part of the EAO.
- (3) The Bure adakitic rock is the product of thickened juvenile crust melting triggered by the Pan-African Orogeny during the Neoproterozoic.

**Author Contributions:** J.J., W.X. and P.H. conceived this contribution and conducted all field and analytical work, assisted by Y.L., F.W., G.Z., X.G., Z.Z. and Y.B. The manuscript was written by J.J., W.X. and P.H., with contribution from Y.L., F.W., G.Z., X.G., Z.Z. and Y.B. All authors have read and agreed to the published version of the manuscript.

**Funding:** J.S.J. acknowledges support from the Natural Science Foundation of Hubei Province of China (2022CFB850), National Natural Science Foundation of China (42202092), Open Fund of the Research Center for Petrogenesis and Mineralization of Granitoid Rocks, China Geological Survey (No. PMGR202018), and the China Geological Survey (DD20221802, DD20230575).

**Data Availability Statement:** Data are contained within the article.

**Acknowledgments:** Staff at Wuhan Sample Solution Analytical Technology Co., Ltd., Zhongnan Mineral Resources Supervision and Test Center for Geoanalysis, Wuhan Center, China Geological Survey are gratefully acknowledged for assistance with instrument operation. We thank the reviewers for the journal Minerals.

**Conflicts of Interest:** Zicheng Zhang is employee of China National Geological & Mining Corporation. The paper reflects the views of the scientists and not the company. The remaining authors declare that the research was conducted in the absence of any commercial or financial relationships that could be construed as a potential conflict of interest.

## References

1. Collins, A.S.; Pisarevsky, S.A. Amalgamating eastern Gondwana: The evolution of the Circum-Indian Orogens. *Earth-Sci. Rev.* **2005**, *71*, 229–270. [[CrossRef](#)]
2. Fritz, H.; Abdelsalam, M.; Ali, K.A.; Bingen, B.; Collins, A.S.; Fowler, A.R.; Ghebreab, W.; Hauzenberger, C.A.; Johnson, P.R.; Kusky, T.M.; et al. Orogen styles in the East African Orogen: A review of the Neoproterozoic to Cambrian tectonic evolution. *J. Afr. Earth Sci.* **2013**, *86*, 65–106. [[CrossRef](#)] [[PubMed](#)]

3. Stern, R.J. Arc-assembly and continental collision in the Neoproterozoic African Orogen: Implications for the consolidation of Gondwanaland. *Annu. Rev. Earth Planet. Sci.* **1994**, *22*, 319–351. [[CrossRef](#)]
4. Abdelsalam, M.; Stern, R. Sutures and shear zones in the Arabian-Nubian Shield. *J. Afr. Earth Sci.* **1996**, *23*, 289–310. [[CrossRef](#)]
5. Ayalew, T.; Peccerillo, A. Petrology and geochemistry of the Gore-Gambella plutonic rocks: Implications for magma genesis and the tectonic setting of the Pan-African Orogenic Belt of western Ethiopia. *J. Afr. Earth Sci.* **1998**, *27*, 397–416. [[CrossRef](#)]
6. Bowden, S.; Gani, N.D.; Alemu, T.; O'Sullivan, P.; Abebe, B.; Tadesse, K. Evolution of the Western Ethiopian Shield revealed through U-Pb geochronology, petrogenesis, and geochemistry of syn- and post-tectonic intrusive rocks. *Precambrian Res.* **2020**, *338*, 105588. [[CrossRef](#)]
7. Jiang, J.S.; Hu, P.; Xiang, W.S.; Wang, J.X.; Lei, Y.J.; Zhao, K.; Zeng, G.P.; Wu, F.F.; Xiang, P. Geochronology, geochemistry and its implication for regional tectonic evolution of adakite-like rock in the Bure area, western Ethiopia. *Acta Geol. Sin.-Engl.* **2021**, *95*, 1260–1272. (In Chinese with English Abstract)
8. Kebede, T.; Koeberl, C.; Koller, F. Geology, geochemistry and petrogenesis of intrusive rocks of the Wallagga area, western Ethiopia. *J. Afr. Earth Sci.* **1999**, *29*, 715–734. [[CrossRef](#)]
9. Kebede, T.; Koeberl, C.; Koller, F. Magmatic evolution of the suqii-wagga garnet-bearing two-mica granite, wallagga area, western Ethiopia. *J. Afr. Earth Sci.* **2001**, *32*, 193–221. [[CrossRef](#)]
10. Woldemichael, B.W.; Kimura, J.; Dunkley, D.J.; Tani, K.; Ohira, H. SHRIMP U-Pb zircon geochronology and Sr-Nd isotopic systematic of the Neoproterozoic Ghimbi-Nedjo mafic to intermediate intrusions of Western Ethiopia: A record of passive margin magmatism at 855 Ma? *Int. J. Earth Sci.* **2010**, *99*, 1773–1790. [[CrossRef](#)]
11. Xiang, W.S.; Jiang, J.S.; Lei, Y.J.; Zhao, K. Petrogenesis of A-type granite and geological significance of Bure area, western Ethiopia. *Earth Sci.* **2021**, *46*, 2299–2310. (In Chinese with English Abstract).
12. Xu, J.F.; Shinji, R.; Defant, M.J.; Wang, Q.; Rapp, R.P. Origin of Mesozoic adakitic intrusive rocks in the Ningzhen area of east China: Partial melting of delaminated lower continental crust? *Geology* **2002**, *30*, 1111–1114. [[CrossRef](#)]
13. Jacobs, J.; Thomas, R.J. Himalayan-type indenter-escape tectonics model for the southern part of the late Neoproterozoic-early Palaeozoic East African Antarctic orogen. *Geology* **2004**, *32*, 721–724. [[CrossRef](#)]
14. Johnson, P.; Andresen, A.; Collins, A.S.; Fowler, A.; Fritz, H.; Ghebreab, W.; Kusky, T.; Stern, R. Late Cryogenian–Ediacaran history of the Arabian-Nubian Shield: A review of depositional, plutonic, structural, and tectonic events in the closing stages of the northern East African Orogen. *J. Afr. Earth Sci.* **2011**, *61*, 167–232. [[CrossRef](#)]
15. Allen, A.; Tadesse, G. Geological setting and tectonic subdivision of the Neoproterozoic orogenic belt of Tulu Dimtu, western Ethiopia. *J. Afr. Earth Sci.* **2003**, *36*, 329–343. [[CrossRef](#)]
16. Cox, G.M.; Lewis, C.J.; Collins, A.S.; Halverson, G.P.; Jourdan, F.; Foden, J.; Nettle, D.; Kattan, F. Ediacaran terrane accretion within the Arabian–Nubian Shield. *Gondwana Res.* **2012**, *21*, 341–352. [[CrossRef](#)]
17. Kröner, A.; Linnebacher, P.; Stern, R.; Reischmann, T.; Manton, W.; Hussein, I. Evolution of Pan-African island arc assemblages in the southern Red Sea Hills, Sudan, and in southwestern Arabia as exemplified by geochemistry and geochronology. *Precambrian Res.* **1991**, *53*, 99–118. [[CrossRef](#)]
18. Robinson, F.; Foden, J.; Collins, A.; Payne, J. Arabian Shield magmatic cycles and their relationship with Gondwana assembly: Insights from zircon U–Pb and Hf isotopes. *Earth Planet. Sci. Lett.* **2014**, *408*, 207–225. [[CrossRef](#)]
19. Shackleton, R. The final collision zone between East and West Gondwana: Where is it? *J. Afr. Earth Sci.* **1996**, *23*, 271–287. [[CrossRef](#)]
20. Meert, J.G. A synopsis of events related to the assembly of eastern Gondwana. *Tectonophysics* **2003**, *362*, 1–40. [[CrossRef](#)]
21. Woldemichael, B.W.; Kimura, J.I. Petrogenesis of the Neoproterozoic Bikilal Ghimbi gabbro, western Ethiopia. *J. Mineral. Petrol. Sci.* **2008**, *103*, 23–46. [[CrossRef](#)]
22. Stern, R.J. Crustal evolution in the East African Orogen: A neodymium isotopic perspective. *J. Afr. Earth Sci.* **2002**, *34*, 109–117. [[CrossRef](#)]
23. Tadesse, G.; Allen, A. Geology and geochemistry of the Neoproterozoic Tulu Dimtu Ophiolite suite, western Ethiopia. *J. Afr. Earth Sci.* **2005**, *41*, 192–211. [[CrossRef](#)]
24. Braathen, A.; Grenne, T.; Selassie, M.; Worku, T. Juxtaposition of Neoproterozoic units along the Baruda–Tulu Dimtu shear-belt in the East African Orogen of western Ethiopia. *Precambrian Res.* **2001**, *107*, 215–234. [[CrossRef](#)]
25. Grenne, T.; Pedersen, R.B.; Bjerkgård, T.; Braathen, A.; Selassie, M.G.; Worku, T. Neoproterozoic evolution of Western Ethiopia: Igneous geochemistry, isotope systematics and U–Pb ages. *Geol. Mag.* **2003**, *140*, 373–395. [[CrossRef](#)]
26. Mogessie, A.; Belete, K.; Hoinkes, G. Yubdo-Tulu Dimtu mafic-ultramafic belt, Alaskan-type intrusions in western Ethiopia: Its implication to the Arabian-Nubian Shield and tectonics of the Mozambique Belt. *J. Afr. Earth Sci.* **2000**, *30*, 62.
27. Blades, M.L.; Collins, A.S.; Foden, J.; Payne, J.L.; Xu, X.; Alemu, T.; Woldetinsae, G.; Clark, C.; Taylor, R.J.M. Age and hafnium isotopic evolution of the Didesa and Kemashi Domains, western Ethiopia. *Precambrian Res.* **2015**, *270*, 267–284. [[CrossRef](#)]
28. Kebede, T.; Koeberl, C. Petrogenesis of A-type granitoids from the Wallagga area, western Ethiopia: Constraints from mineralogy, bulk-rock chemistry, Nd and Sr isotopic compositions. *Precambrian Res.* **2003**, *121*, 1–24. [[CrossRef](#)]
29. Liu, Y.S.; Hu, Z.C.; Gao, S.; Günther, D.; Xu, J.; Gao, C.G.; Chen, H.H. In situ analysis of major and trace elements of anhydrous minerals by LA-ICP-MS without applying an internal standard. *Chem. Geol.* **2008**, *257*, 34–43. [[CrossRef](#)]

30. Qiu, X.-F.; Ling, W.-L.; Liu, X.-M.; Kusky, T.; Berkana, W.; Zhang, Y.-H.; Gao, Y.-J.; Lu, S.-S.; Kuang, H.; Liu, C.-X. Recognition of Grenvillian volcanic suite in the Shennongjia region and its tectonic significance for the South China Craton. *Precambrian Res.* **2011**, *191*, 101–119. [[CrossRef](#)]
31. Hu, Z.C.; Liu, Y.S.; Gao, S.; Liu, W.; Yang, L.; Zhang, W.; Tong, X.; Lin, L.; Zong, K.Q.; Li, M.; et al. Improved in situ Hf isotope ratio analysis of zircon using newly designed X skimmer cone and jet sample cone in combination with the addition of nitrogen by laser ablation multiple collector ICP-MS. *J. Anal. At. Spectrom.* **2012**, *27*, 1391–1399. [[CrossRef](#)]
32. Fisher, C.M.; Vervoort, J.D.; Hanchar, J.M. Guidelines for reporting zircon Hf isotopic data by LA-MC-ICPMS and potential pitfalls in the interpretation of these data. *Chem. Geol.* **2014**, *363*, 125–133. [[CrossRef](#)]
33. Liu, Y.S.; Gao, S.; Hu, Z.C.; Gao, C.G.; Zong, K.Q.; Wang, D.B. Continental and oceanic crust recycling-induced melt-peridotite interactions in the Trans-North China Orogen: U–Pb dating, Hf isotopes and trace elements in zircons of mantle xenoliths. *J. Petrol.* **2010**, *51*, 537–571. [[CrossRef](#)]
34. Zhang, W.; Hu, Z. Estimation of Isotopic Reference Values for Pure Materials and Geological Reference Materials. *At. Spectrosc.* **2020**, *41*, 93–102. [[CrossRef](#)]
35. Chen, G.Y.; Sun, D.S.; Zhou, X.R.; Shao, W.; Gong, R.T.; Shao, Y. *Mineralogy of Guojialing Granodiorite and Its Relationship to Gold Mineralization in the Jiaodong Peninsula*; Chinese University of Geosciences: Beijing, China, 1993; pp. 1–230.
36. Deer, W.A.; Howie, R.A.; Zussman, J. *An Introduction to the Rock Forming Minerals*, 2nd ed.; Longman Group: Harlow, UK, 1992; pp. 1–232.
37. Foster, M.D. *Interpretation of the Composition of Trioctahedral Mica*; U.S. Geological Survey Professional Paper 354-B; U.S. Government Printing Office: Washington, DC, USA, 1960; pp. 11–48.
38. Lin, W.W.; Peng, L.J. Estimation of Fe<sup>3+</sup> and Fe<sup>2+</sup> in hornblende and biotite by electron probe analysis data. *J. Chang. Coll. Geol.* **1994**, *24*, 155–162.
39. Kumar, S.; Pathak, M. Mineralogy and geochemistry of biotites from Proterozoic granitoids of western Arunachal Himalaya: Evidence of bimodal granitogeny and tectonic affinity. *J. Geol. Soc. India* **2010**, *75*, 715–730. [[CrossRef](#)]
40. Guo, Y.Y.; He, W.Y.; Li, Z.C.; Ji, X.Z.; Han, Y.; Fang, W.K.; Yin, C. Petrogenesis of Ge'erkuohe porphyry granitoid, western Qinling: Constraints from mineral chemical characteristics of biotites. *Acta Petrol. Sin.* **2015**, *31*, 3380–3390. (In Chinese with English Abstract)
41. Hoskin, P.W. Trace-element composition of hydrothermal zircon and the alteration of Hadean zircon from the Jack Hills, Australia. *Geochim. Cosmochim. Acta* **2005**, *69*, 637–648. [[CrossRef](#)]
42. Watson, E.B.; Harrison, T.M. Zircon Thermometer Reveals Minimum Melting Conditions on Earliest Earth. *Science* **2005**, *308*, 841–844. [[CrossRef](#)]
43. Ballard, J.R.; Palin, M.J.; Campbell, I.H. Relative oxidation states of magmas inferred from Ce (IV)/Ce (III) in zircon: Application to porphyry copper deposits of northern Chile. *Contrib. Mineral. Petrol.* **2002**, *144*, 347–364. [[CrossRef](#)]
44. Trail, D.; Watson, E.B.; Tailby, N.D. Ce and Eu anomalies in zircon as proxies for the oxidation state of magmas. *Geochim. Cosmochim. Acta* **2012**, *97*, 70–87. [[CrossRef](#)]
45. Li, W.K.; Cheng, Y.Q.; Yang, Z.M. Geo-fO<sub>2</sub>: Integrated software for analysis of magmatic oxygen fugacity. *Geochem. Geophys. Geosy.* **2019**, *20*, 2542–2555. [[CrossRef](#)]
46. Sun, S.S.; McDonough, W.F. Chemical and isotopic systematics of oceanic basalts: Implications for mantle composition and processes. *Geol. Soc. Lond. Spec. Publ.* **1989**, *42*, 313–345. [[CrossRef](#)]
47. Bouvier, A.; Blichert-Toft, J.; Vervoort, J.D.; Gillet, P.; Albarède, F. The case for old basaltic shergottites. *Earth Planet. Sci. Lett.* **2008**, *266*, 105–124. [[CrossRef](#)]
48. Wasserburg, G.J.; Jacobsen, S.B.; DePaolo, D.J.; McCulloch, M.T.; Wen, T. Precise determination of SmNd ratios, Sm and Nd isotopic abundances in standard solutions. *Geochim. Cosmochim. Acta* **1981**, *45*, 2311–2323. [[CrossRef](#)]
49. Liew, T.C.; Hofmann, A.W. Precambrian crustal components, plutonic associations, plate environment of the Hercynian Fold Belt of central Europe: Indications from a Nd and Sr isotopic study. *Contrib. Mineral. Petrol.* **1988**, *98*, 129–138. [[CrossRef](#)]
50. Jahn, B.-M.; Condie, K.C. Evolution of the Kaapvaal Craton as viewed from geochemical and Sm-Nd isotopic analyses of intracratonic pelites. *Geochim. Cosmochim. Acta* **1995**, *59*, 2239–2258. [[CrossRef](#)]
51. Khan, J.; Yao, H.-Z.; Zhao, J.-H.; Tahir, A.; Chen, K.-X.; Wang, J.-X.; Song, F.; Xu, J.-Y.; Shah, I. Geochronology, geochemistry, and tectonic setting of the Neoproterozoic magmatic rocks in Pan-African basement, West Ethiopia. *Ore Geol. Rev.* **2024**, *164*, 105858. [[CrossRef](#)]
52. Manda, B.W.; Cawood, P.A.; Spencer, C.J.; Prave, T.; Robinson, R.; Roberts, N.M.W. Evolution of the Mozambique Belt in Malawi constrained by granitoid U–Pb, Sm–Nd and Lu–Hf isotopic data. *Gondwana Res.* **2018**, *68*, 93–107. [[CrossRef](#)]
53. Griffin, W.; Graham, S.; O'Reilly, S.Y.; Pearson, N. Lithosphere evolution beneath the Kaapvaal Craton: Re–Os systematics of sulfides in mantle-derived peridotites. *Chem. Geol.* **2004**, *208*, 89–118. [[CrossRef](#)]
54. Pearce, J.A.; Harris, N.B.W.; Tindle, A.G. Trace Element Discrimination Diagrams for the Tectonic Interpretation of Granitic Rocks. *J. Petrol.* **1984**, *25*, 956–983. [[CrossRef](#)]
55. Zeng, G.P.; Wang, J.X.; Xiang, W.S.; Zhang, Z.C.; Jiang, J.S.; Xiang, P. The Augaro Arc-type Granite in the Nubia Shield, Western Eritrea: Petrogenesis and Implications for Neoproterozoic Geodynamic Evolution of the East African Orogen. *Northwestern Geol.* **2024**, *57*, 159–173. (In Chinese with English abstract)

56. Uchida, E.; Endo, S.; Makino, M. Relationship Between Solidification Depth of Granitic Rocks and Formation of Hydrothermal Ore Deposits. *Resour. Geol.* **2007**, *57*, 47–56. [[CrossRef](#)]
57. Wones, D.R.; Eugster, H.P. Stability of biotite: Experiment, theory, and application. *Am. Mineral.* **1965**, *50*, 1228–1272.
58. Jiang, J.-S.; Zheng, Y.-Y.; Gao, S.-B.; Zhang, Y.-C.; Huang, J.; Liu, J.; Wu, S.; Xu, J.; Huang, L.-L. The newly-discovered Late Cretaceous igneous rocks in the Nuocang district: Products of ancient crust melting triggered by Neo–Tethyan slab rollback in the western Gangdese. *Lithos* **2018**, *308–309*, 294–315. [[CrossRef](#)]
59. Loader, M.A.; Nathwani, C.L.; Wilkinson, J.J.; Armstrong, R.N. Controls on the magnitude of Ce anomalies in zircon. *Geochim. Cosmochim. Acta* **2022**, *328*, 242–257. [[CrossRef](#)]
60. Teklay, M.; Kröner, A.; Mezger, K.; Oberhänsli, R. Geochemistry, Pb Pb single zircon ages and Nd Sr isotope composition of Precambrian rocks from southern and eastern Ethiopia: Implications for crustal evolution in East Africa. *J. Afr. Earth Sci.* **1998**, *26*, 207–227. [[CrossRef](#)]
61. Kröner, A.; Sassi, F.P. Evolution of the northern Somali basement: New constraints from zircon ages. *J. Afr. Earth Sci.* **1996**, *22*, 1–15. [[CrossRef](#)]
62. Harris, N.B.W.; Marzouki, F.M.H.; Ali, S. The Jabel Sayid complex, Arabian Shield: Geochemical constraints on the origin of peralkaline and related granites. *J. Geol. Soc.* **1986**, *143*, 287–295. [[CrossRef](#)]
63. Stern, R.J.; Kröner, A. Late Precambrian Crustal Evolution in NE Sudan: Isotopic and Geochronologic Constraints. *J. Geol.* **1993**, *101*, 555–574. [[CrossRef](#)]
64. Stern, R.J.; Abdelsalam, M.G. Formation of juvenile continental crust in the Arabian-Nubian Shield, evidence from granitic rocks of the Nakasib suture, NE Sudan. *Geol. Rundsch.* **1998**, *87*, 150–160. [[CrossRef](#)]
65. Zeng, G.P.; Wang, J.X.; Xiang, W.S.; Tong, X.R.; Shao, X.; Hu, P.; Wu, F.F.; Jiang, J.S.; Xiang, P. Petrogenesis and Geological Significance of the Adi Keyh A-type Rhyolite in Central Eritrea. *South China Geol.* **2022**, *38*, 157–173. (In Chinese with English)
66. Abdel-Rahman, A.F.M. Nature of biotites from alkaline, calcalkaline, and peraluminous magmas. *J. Petrol.* **1994**, *35*, 525–541. [[CrossRef](#)]
67. Zhou, Z.X. The origin of intrusive mass in Fengshandong, Hubei Province. *Acta Petrol. Sin.* **1986**, *2*, 59–70. (In Chinese with English)
68. Defant, M.J.; Drummond, M.S. Derivation of some modern arc magmas by melting of young subducted lithosphere. *Nature* **1990**, *347*, 662–665. [[CrossRef](#)]
69. Schulz, B.; Klemm, R.; Brätz, H. Host rock compositional controls on zircon trace element signatures in metabasites from the Au-stroalpine basement. *Geochim. Cosmochim. Acta* **2006**, *70*, 697–710. [[CrossRef](#)]

**Disclaimer/Publisher’s Note:** The statements, opinions and data contained in all publications are solely those of the individual author(s) and contributor(s) and not of MDPI and/or the editor(s). MDPI and/or the editor(s) disclaim responsibility for any injury to people or property resulting from any ideas, methods, instructions or products referred to in the content.